



## Aircraft measurements of BrO, IO, glyoxal, NO<sub>2</sub>, H<sub>2</sub>O, O<sub>2</sub>–O<sub>2</sub> and aerosol extinction profiles in the tropics: comparison with aircraft-/ship-based in situ and lidar measurements

R. Volkamer<sup>1,2</sup>, S. Baidar<sup>1,2</sup>, T. L. Campos<sup>3</sup>, S. Coburn<sup>1,2</sup>, J. P. DiGangi<sup>4,\*</sup>, B. Dix<sup>1</sup>, E. W. Eloranta<sup>5</sup>, T. K. Koenig<sup>1,2</sup>, B. Morley<sup>6</sup>, I. Ortega<sup>1,2</sup>, B. R. Pierce<sup>7</sup>, M. Reeves<sup>6</sup>, R. Sinreich<sup>1</sup>, S. Wang<sup>1,2,\*\*</sup>, M. A. Zondlo<sup>4</sup>, and P. A. Romashkin<sup>6</sup>

<sup>1</sup>Department of Chemistry & Biochemistry, University of Colorado, Boulder, CO, USA

<sup>2</sup>Cooperative Institute for Research in Environmental Sciences (CIRES), University of Colorado, Boulder, CO, USA

<sup>3</sup>National Center for Atmospheric Research (NCAR), Atmospheric Chemistry Division (ACD), Boulder, CO, USA

<sup>4</sup>Department of Civil and Environmental Engineering, Princeton University, Princeton, NJ, USA

<sup>5</sup>Space Science and Engineering Center, University of Wisconsin, Madison, WI, USA

<sup>6</sup>National Center for Atmospheric Research (NCAR), Research Aviation Facility/Earth Observing Laboratory (RAF/EOL), Broomfield, CO, USA

<sup>7</sup>National Oceanic and Atmospheric Administration (NOAA), The National Environmental Satellite, Data, and Information Service (NESDIS), Madison, WI, USA

\* now at: National Aeronautics and Space Administration (NASA) Langley Research Center, Hampton, VA, USA

\*\* now at: Department of Chemistry, Hong Kong University of Science and Technology, Hong Kong, China

Correspondence to: R. Volkamer (rainer.volkamer@colorado.edu)

Received: 18 December 2014 – Published in Atmos. Meas. Tech. Discuss.: 19 January 2015

Revised: 1 April 2015 – Accepted: 10 April 2015 – Published: 20 May 2015

**Abstract.** Tropospheric chemistry of halogens and organic carbon over tropical oceans modifies ozone and atmospheric aerosols, yet atmospheric models remain largely untested for lack of vertically resolved measurements of bromine monoxide (BrO), iodine monoxide (IO) and small oxygenated hydrocarbons like glyoxal (CHOCHO) in the tropical troposphere. BrO, IO, glyoxal, nitrogen dioxide (NO<sub>2</sub>), water vapor (H<sub>2</sub>O) and O<sub>2</sub>–O<sub>2</sub> collision complexes (O<sub>4</sub>) were measured by the University of Colorado Airborne Multi-AXis Differential Optical Absorption Spectroscopy (CU AMAX-DOAS) instrument, aerosol extinction by high spectral resolution lidar (HSRL), in situ aerosol size distributions by an ultra high sensitivity aerosol spectrometer (UHSAS) and in situ H<sub>2</sub>O by vertical-cavity surface-emitting laser (VCSEL) hygrometer. Data are presented from two research flights (RF12, RF17) aboard the National Science Foundation/National Center for Atmospheric Research Gulfstream V aircraft over the tropical Eastern Pacific Ocean (tEPO) as part of the “Tropical Ocean Troposphere Exchange of Reactive halogens and Oxygenated hydrocarbons” (TORERO)

project (January/February 2012). We assess the accuracy of O<sub>4</sub> slant column density (SCD) measurements in the presence and absence of aerosols. Our O<sub>4</sub>-inferred aerosol extinction profiles at 477 nm agree within 6 % with HSRL in the boundary layer and closely resemble the renormalized profile shape of Mie calculations constrained by UHSAS at low (sub-Rayleigh) aerosol extinction in the free troposphere. CU AMAX-DOAS provides a flexible choice of geometry, which we exploit to minimize the SCD in the reference spectrum (SCD<sub>REF</sub>, maximize signal-to-noise ratio) and to test the robustness of BrO, IO and glyoxal differential SCDs. The RF12 case study was conducted in pristine marine and free tropospheric air. The RF17 case study was conducted above the NOAA RV *Ka'imimoana* (TORERO cruise, KA-12-01) and provides independent validation data from ship-based in situ cavity-enhanced DOAS and MAX-DOAS. Inside the marine boundary layer (MBL) no BrO was detected (smaller than 0.5 pptv), and 0.2–0.55 pptv IO and 32–36 pptv glyoxal were observed. The near-surface concentrations agree within 30 % (IO) and 10 % (glyoxal) between ship and air-

craft. The BrO concentration strongly increased with altitude to 3.0 pptv at 14.5 km (RF12, 9.1 to 8.6° N; 101.2 to 97.4° W). At 14.5 km, 5–10 pptv NO<sub>2</sub> agree with model predictions and demonstrate good control over separating tropospheric from stratospheric absorbers (NO<sub>2</sub> and BrO). Our profile retrievals have 12–20 degrees of freedom (DoF) and up to 500 m vertical resolution. The tropospheric BrO vertical column density (VCD) was  $1.5 \times 10^{13}$  molec cm<sup>-2</sup> (RF12) and at least  $0.5 \times 10^{13}$  molec cm<sup>-2</sup> (RF17, 0–10 km, lower limit). Tropospheric IO VCDs correspond to  $2.1 \times 10^{12}$  molec cm<sup>-2</sup> (RF12) and  $2.5 \times 10^{12}$  molec cm<sup>-2</sup> (RF17) and glyoxal VCDs of  $2.6 \times 10^{14}$  molec cm<sup>-2</sup> (RF12) and  $2.7 \times 10^{14}$  molec cm<sup>-2</sup> (RF17). Surprisingly, essentially all BrO as well as the dominant IO and glyoxal VCD fraction was located above 2 km (IO:  $58 \pm 5$  %, 0.1–0.2 pptv; glyoxal:  $52 \pm 5$  %, 3–20 pptv). To our knowledge there are no previous vertically resolved measurements of BrO and glyoxal from aircraft in the tropical free troposphere. The atmospheric implications are briefly discussed. Future studies are necessary to better understand the sources and impacts of free tropospheric halogens and oxygenated hydrocarbons on tropospheric ozone, aerosols, mercury oxidation and the oxidation capacity of the atmosphere.

## 1 Introduction

Tropospheric halogens, like bromine and iodine, destroy ozone and oxidize atmospheric mercury and affect oxidative capacity ( $\text{HO}_x = \text{OH} + \text{HO}_2$ ) (Parrella et al., 2012; Saiz-Lopez et al., 2012a). Glyoxal, the smallest  $\alpha$ -dicarbonyl, is an indicator for hydrocarbon oxidation (Volkamer et al., 2005a) on global scales (Wittrock et al., 2006; Vrekoussis et al., 2009; Lerot et al., 2010) and a precursor for the formation of secondary organic aerosol (SOA) (Carlton et al., 2007; Fu et al., 2008; Kampf et al., 2013; Waxman et al., 2013; Knote et al., 2014; Kurtén et al., 2014). Atmospheric models currently remain largely untested for BrO, IO and glyoxal vertical distributions at tropical latitudes largely due to the extreme scarcity of vertically resolved measurements. Such measurements are particularly important in the tropics, where about 75 % of the chemical removal of the greenhouse gases methane (CH<sub>4</sub>) and ozone (O<sub>3</sub>) occurs (Lelieveld et al., 1998; Saiz-Lopez et al., 2012a) and where changes in O<sub>3</sub> show a particular climate sensitivity (Mickley et al., 2004). Vertical profile measurements of BrO, IO and glyoxal in the tropical troposphere pose unique constraints to atmospheric models and are further relevant for the interpretation of satellites data.

Airborne Multi-AXis DOAS (AMAX-DOAS) measurements can provide profile information about trace gases and aerosol extinction from limb measurements of scattered sunlight spectra from aircraft. The AMAX-DOAS technique has been used to measure tropospheric NO<sub>2</sub> (Melamed et al.,

2003; Heue et al., 2005; Wang et al., 2005; Bruns et al., 2006; Dix et al., 2009; Merlaud et al., 2011, 2012; Oetjen et al., 2013; Baidar et al., 2013a), sulfur dioxide (SO<sub>2</sub>) (Wang et al., 2006; Melamed et al., 2008; Heue et al., 2011), nitrous acid (HONO) (Dix et al., 2009; Heue et al., 2014), BrO (Dix et al., 2009; Heue et al., 2011; Prados-Roman et al., 2011), IO (Dix et al., 2013), formaldehyde (HCHO) (Dix et al., 2009; Baidar et al., 2013a; Heue et al., 2014) and glyoxal (Baidar et al., 2013a). However, no reports of BrO, IO and glyoxal currently exist using this technique at tropical latitudes. Furthermore, the AMAX-DOAS technique has not been extensively evaluated for gases other than NO<sub>2</sub>. Aerosol extinction profiles are prerequisites to retrievals of trace-gas profiles and can be inferred from observations of the oxygen collision complex, O<sub>2</sub>-O<sub>2</sub> (O<sub>4</sub>) (Wagner et al., 2004) or radiance-based retrievals (Prados-Roman et al., 2011). However, to our knowledge the evaluation of aerosol extinction profiles from AMAX-O<sub>4</sub> limb measurements by means of High Spectral Resolution Lidar (HSRL) and/or vertically resolved in situ measurements of aerosols has not been attempted before.

The CU AMAX-DOAS instrument is designed to maximize sensitivity and vertical resolution during limb observations from aircraft (Baidar et al., 2013a). The instrument has been compared with NO<sub>2</sub> vertical columns under polluted/semi-polluted conditions (Oetjen et al., 2013; Baidar et al., 2013a) and used to test NO<sub>x</sub> emission inventories in atmospheric models (Baidar et al., 2013b). Furthermore, the accuracy of O<sub>4</sub> measurements has recently been assessed in a pure Rayleigh atmosphere (Spinei et al., 2015). However, no previous evaluations have been performed using vertically resolved information. A series of research flights were conducted as part of the Tropical Ocean tRoposphere Exchange of Reactive halogen species and Oxygenated volatile organic compound (VOC) project (TORERO) (18 January–29 February 2012) using a comprehensive payload of chemical in situ and remote sensing instruments aboard the National Science Foundation/National Center for Atmospheric Research Gulfstream V aircraft (NSF/NCAR GV) to study the release, transport and fate of reactive halogen gases and oxidized VOCs over the tropical Eastern Pacific Ocean (tEPO). The aircraft deployment was coordinated with the NOAA RV *Ka'imimoana* cruise from Hawaii to Puntarenas, Costa Rica (KA-12-01 – TORERO cruise) (Coburn et al., 2014). The TORERO data set provides an excellent opportunity to evaluate the robustness of DOAS retrievals and compare with aerosol extinction profiles constrained from in situ measurements of aerosol size distributions, as well as in situ H<sub>2</sub>O profiles measured on the NSF/NCAR GV. We also compare IO and glyoxal aircraft profiles with a ship MAX-DOAS instrument (Sinreich et al., 2010) aboard NOAA RV *Ka'imimoana* and near-surface concentrations of glyoxal by the in situ fast light-emitting-diode cavity-enhanced DOAS (fast LED-CE-DOAS) instrument (Coburn et al., 2014). Only selected case studies can be discussed here, but the methods

for AMAX profile retrievals are applicable for the evaluation of other TORERO flights (total of 17 research flights). TORERO is a US contribution to the Surface Ocean Lower Atmosphere Study (SOLAS) project.

## 2 Experimental

The TORERO cruise track of the RV *Ka'imimoana*, and flight tracks of TORERO research flights RF12 and RF17 are shown in Fig. 1. The objective of RF12 was to measure BrO profiles in the upper tropical free troposphere (FT) under pristine conditions and over the maximum accessible altitude range of the NSF/NCAR GV aircraft (0.1 to 14.5 km). RF17 was optimized to characterize the chemical and radiation state of the atmosphere above the ship. RF17 is used here to compare the data from in situ and remote sensing instruments in the lower atmosphere (up to 2 km). The GV aircraft conducted a “flyby” near the ship and measured vertical profiles of BrO, IO and glyoxal mixing ratios up to 10.5 km. These vertical profiles complement the boundary layer observations with information about atmospheric composition aloft. Results discussed in this study used the following instruments, methods and models.

### 2.1 CU AMAX-DOAS instrument

BrO, IO, glyoxal, NO<sub>2</sub>, H<sub>2</sub>O and O<sub>4</sub> vertical profiles were measured by limb observations, i.e., elevation angle (EA) 0, of scattered solar photons. The CU AMAX-DOAS instrument, its data analysis and profile retrieval methods have been described in detail elsewhere (Oetjen et al., 2013; Dix et al., 2013; Baidar et al., 2013a). Briefly, the instrument measures scattered sunlight spectra from well-defined lines of sight (elevation angles), which are defined above (positive EA), below (negative EA) and forward of the aircraft (0 EA is limb geometry). The limb scanning telescope has a vertical dispersion of 0.17° and is actively angle stabilized to an accuracy better than 0.2° in real time. Two synchronized spectrograph–detector units (Acton SP2150/PIXIS400B CCD, 1340 × 400 pixels or 26.8 × 8 mm) simultaneously observed the spectral ranges from 330 to 470 nm (BrO, IO, glyoxal, NO<sub>2</sub>, H<sub>2</sub>O and O<sub>4</sub> at 360 nm; 0.7 nm full width half maximum (FWHM) optical resolution) and 440 to 700 nm (O<sub>4</sub> at 477 nm; 1.2 nm FWHM optical resolution). During the profile case studies the aircraft was changing altitude at a rate of 457–914 m min<sup>-1</sup> at constant heading between 0.1 and 14.5 km. AMAX-DOAS was recording limb spectra with an integration time of 60 s for the BrO case study of RF12, and 30 s integration time was used for the ship comparison during RF17. Typical detection limits in the FT/MBL are 0.3/0.6 pptv BrO, 0.04/0.1 pptv IO, 3/7 pptv glyoxal, 5/10 pptv NO<sub>2</sub> and 50/120 ppmv H<sub>2</sub>O, where 1 pptv is 1 parts per trillion by

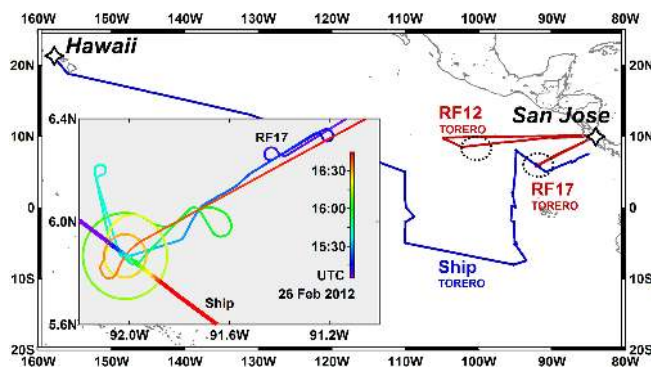


**Figure 1.** TORERO cruise track (blue line) and GV flight tracks (red lines), where the locations of the RF12 and RF17 profile case studies are indicated (dashed circle). The inset shows the detailed view of the flight track during the instrument intercomparison above the RV *Ka'imimoana* (RF17).

volume  $\approx 2.46 \times 10^7$  molec cm<sup>-3</sup> (101 325 Pa, 298 K) and 1 pptv = 10<sup>3</sup> ppbv = 10<sup>6</sup> pptv.

### 2.2 High spectral resolution lidar aboard the GV

The HSRL provides vertical profiles of backscatter cross section, extinction cross section and depolarization (Shiple et al., 1983; Piironen and Eloranta, 1994; Eloranta, 2005). The HSRL separates molecular and particulate scattering into independent profiles. Dividing the particulate backscatter profile by the molecular profile provides a scattering ratio profile. This ratio cancels out atmospheric attenuation and range-dependent lidar gain effects. The ratio can be used with an independently supplied profile of atmospheric density to compute a robustly calibrated profile of particulate backscatter. The extinction cross section is derived from attenuation of the molecular signal relative to the expected molecular return from a clear atmosphere. Because extinction depends on the rate of decrease of the molecular signal it involves a differentiation which increases signal noise. Close to the lidar range-dependent focus errors can produce large changes in system sensitivity. During RF17 two extinction profiles were measured at 532 nm below the aircraft (14:40–14:49 and 16:48–16:59 UTC); these periods were chosen to minimize range-dependent focus errors, avoid clouds and characterize atmospheric variability before and after the ship interception. Some remaining scattered low clouds during the above periods were removed by application of a cloud mask. The resulting HSRL error for the extinction measurement is  $\sim 0.01$  km<sup>-1</sup>. For the comparison with O<sub>4</sub>-inferred extinction we have used the average HSRL extinction profile and an Angstrom exponent of 1.26 to calculate extinction at 477 nm.

### 2.3 Aerosol size distribution measurements aboard the GV and Mie calculations

Aerosol size distributions were measured in situ aboard the NSF/NCAR GV by an ultra high sensitivity aerosol spectrometer (UHSAS, airborne model manufactured by DMT, Inc). The UHSAS measures the concentration of particles from 0.06 to 1.0  $\mu\text{m}$  diameter, resolved in 99 size bins, by the technique of laser light scattering. The wing-mounted probe operates in the free stream. A diffusing inlet with a 10:1 deceleration ratio for isokinetic matching of flow serves for sample intake. At typical GV Mach numbers (ranging 0.4 to 0.8), this slowing produces heat from 8 to 30 K. The evaporation of water and other volatile compounds from the particles is minimized by fast delivery to the detection chamber (200 ms delay), but some degree of loss prior to detection cannot be ruled out. The UHSAS is designed to have a nearly linear response with log of particle diameter and to minimize sizing sensitivity to variations in particle refractive index over its size range. The uncertainties in sizing and concentration are 10 and 5 %, respectively. A detailed description of the instrument and its performance is given by Cai et al. (2008).

We have calculated aerosol extinction with a Mie Code that was constrained by these size distributions of accumulation mode sized particles (60 nm to 1.0  $\mu\text{m}$  diameter) and used to estimate the aerosol extinction at the O<sub>4</sub> wavelengths. Sensitivity studies were performed using refractive index,  $n$ , representative of sea salt ( $\sim 1.55$ ) and ice ( $\sim 1.30$ ), assuming constant  $n$  at all sizes, and wavelength dependencies as described in Massie and Hervig (2013). The average aerosol extinction values between 0–2 and 2–10 km were 0.144 and 0.027  $\text{km}^{-1}$  (360 nm) and 0.104 and 0.019  $\text{km}^{-1}$  (477 nm) during RF12 and 0.159 and 0.014  $\text{km}^{-1}$  (360 nm) and 0.122 and 0.010  $\text{km}^{-1}$  (477 nm) during RF17, respectively. The average aerosol size distribution over these altitude ranges had an effective radius:  $R_e = 0.134$  and  $0.110 \pm 0.012 \mu\text{m}$  (RF12) and  $R_e = 0.148$  and  $0.126 \pm 0.014 \mu\text{m}$  (RF17).

### 2.4 Vertical-cavity surface-emitting laser (VCSEL) hygrometer aboard the GV

In situ H<sub>2</sub>O was measured by VCSEL hygrometer aboard the NSF/NCAR GV (Zondlo et al., 2010). The VCSEL hygrometer employs tunable diode laser absorption spectroscopy to determine the water vapor number density over a dew-point range of  $-90$  to  $+30$  °C. It reports the water vapor number density and approximate dew point at 25 samples per second. The hygrometer operates in two absorption modes on two wavelengths: wavelength modulation on a weak absorption line (1853.3 nm, used for high mixing ratio conditions), direct absorption on a strong line (1854.0 nm for moderately low mixing ratios) and wavelength modulation on the strong line (for low mixing ratios). The sample volume is an open-path Herriott cell, giving an absorption length of 375 cm in

a volume approximately 20 cm long and 2 cm in diameter. The sensor was mounted on an adapter plate on top of the NSF/NCAR GV aircraft.

### 2.5 University of Colorado ship MAX-DOAS (CU SMAX-DOAS) instrument aboard RV *Ka'imimoana*

The University of Colorado SMAX-DOAS instrument consists of a telescope, spectrograph/detector units and a laptop PC. The telescope collects scattered sunlight and was mounted on the “experiment platform” in the back of the *Ka'imimoana*. The telescope is comprised of a rotating quartz prism and a quartz lens (cone angle of 0.3°). It is described in more detail in (Sinreich et al., 2010). Two inclinometers are used to motion-control the telescope pointing and keep EA constant during spectra acquisition. Spectra of scattered sunlight were acquired from the EA sequence +90, +0.25, +0.6, +1.5, +3.8, +10, +25, +90 portside and starboard of the ship. The instrument telescope was coupled to a Princeton Instruments Acton SP2300 Czerny–Turner imaging spectrometer with a PIXIS 400B CCD detector. The spectrometer utilized a custom 500  $\text{gmm}^{-1}$  grating blazed at 300 nm and gave simultaneous coverage from 321.3 to 488.4 nm, with 0.74 nm FWHM resolution (Coburn et al., 2011). We use spectra recorded in the portside direction that was closer to the GV overpass for comparison with the AMAX-DOAS during RF17.

### 2.6 LED-CE-DOAS aboard RV *Ka'imimoana*

The fast LED-CE-DOAS instrument is a multispectral sensor that selectively and simultaneously measures glyoxal, O<sub>4</sub> and other gases with 2 Hz time resolution (Coburn et al., 2014). It has a precision of 40 pptv  $\text{Hz}^{-0.5}$  for glyoxal, which corresponds to a detection limit smaller than 2.5 pptv within 1 hour. The instrument is based on an earlier prototype (Thalman and Volkamer, 2010) in which a high-power blue LED (LedEngin model number LZ1-00B205; peak optical power 1.3 W, peak emission near 465 nm) is coupled into a confocal optical cavity equipped with custom coated mirrors (peak reflectivity  $R = 0.999972$ , Advanced Thin Films). The cavity has a base length of 86 cm (74.45 cm sample path length) and was coupled to a Princeton Instruments Acton SP2156 Czerny–Turner imaging spectrometer with a PIXIS 400B CCD. The spectrometer utilized a custom 1000  $\text{gmm}^{-1}$  grating blazed at 250 nm which covered the wavelength range of 390–530 nm with 0.75 nm FWHM resolution. For further details see Coburn et al. (2014).

### 2.7 DOAS analysis

The spectra from the AMAX and SMAX instruments were analyzed using the DOAS method (Platt and Stutz, 2008) and the WinDOAS software package (Fayt and Van Roozendael, 2001). Trace-gas absorption cross-section spectra were

adjusted for resolution, and multiple gases were retrieved simultaneously using nonlinear least-squares fitting routines in a finite wavelength window. The analysis settings and a list of simultaneously fitted cross section reference spectra of atmospheric trace gases are listed in Table 1. Broad band extinction caused by Rayleigh- and Mie-scattering is accounted for by a polynomial fitted simultaneously. For AMAX-DOAS a fixed reference spectrum is used during analysis (see also below). For SMAX-DOAS a zenith spectrum serves as reference, which is updated for each angle scan sequence (see Table 2). The reference spectra eliminate Fraunhofer lines from the solar atmosphere and correct for stratospheric trace gases like NO<sub>2</sub> and O<sub>3</sub>; the cross sections of these two gases were I<sub>0</sub> corrected. A linear intensity offset to correct for instrumental stray light and Ring spectra, modeled with the MFC software (Gomer et al., 1993) (AMAX, Ring 1,2) or DOASIS software (Kraus, 2006) (SMAX, Ring1), and Raman spectrum (Langford et al., 2007) for the AMAX IO were included to correct for inelastic scattering processes. Imperfections in the water cross-section spectra (HITEMP, Rothman et al., 2010, 2013; HITRAN) were explored in the form of further sensitivity studies that included/excluded a water residuum (Sect. 3.2.2, Supplement). The output from the DOAS fit is the differential slant column density (dSCD), i.e., the concentration integral along the light path with respect to a reference spectrum. For information on the LED-CE-DOAS analysis, refer to Coburn et al. (2014).

BrO dSCDs were evaluated using a three-band analysis (Table 1) that was compared to the Aliwell settings (see Sect. 3.2.2). BrO was estimated conservatively in this study by using a “cold” (228 K) BrO cross-section reference spectrum to evaluate our spectra for BrO. This cold spectrum was applied to BrO at warmer temperatures (typical of the lower FT) where the BrO cross section was lower (~20% between 298 and 228 K) (Wilmouth et al., 1999). The bias in BrO concentrations in this paper was essentially 0 in the upper FT, but BrO could be up to ~10% higher in the lower FT. Thus, BrO concentrations should be regarded as lower limits. Aircraft IO analysis settings were very similar to those we had used previously (Dix et al., 2013). The only difference was a slight change in the analysis window (Table 1) based on additional sensitivity studies (Supplement).

### Reference spectra and trace-gas dSCDs

The CU AMAX-DOAS instrument provides a flexible choice of reference spectra. Several references were tested to investigate the sensitivity of the dSCD results with respect to choice of reference and to optimize the resulting dSCDs (see Sect. 3.2.1). With the settings described in Table 1 we have derived BrO, IO, glyoxal, NO<sub>2</sub>, H<sub>2</sub>O and O<sub>4</sub> dSCDs from limb-viewing spectra using reference spectra from EA – 10, EA0 and EA + 10 while the aircraft was near ceiling altitude and from EA + 90 and EA0 in the MBL (0.1 km altitude), as described in Table 2. For BrO we used an EA0 reference

spectrum recorded in the MBL for final analysis because of the higher photon count in these spectra compared to the zenith and the lack of evidence for MBL-BrO in either the ship or aircraft data (see Sect. 4.4.1). Evaluations that used a MBL EA + 90 resulted in slightly higher RMS but identical BrO dSCDs within small error.

The final IO analysis used an EA0 spectrum recorded at 14.5 km as reference spectrum. This geometry has the lowest IO SCD in the reference spectrum (SCD<sub>REF</sub>) and a reasonably high photon count such that the reference spectrum is not limiting the RMS (Coburn et al., 2011) when it is used for the analysis of limb spectra. RF12 and RF17 IO dSCDs were evaluated using this same reference spectrum (Table 2). The IO dSCDs were found to be consistent for reference spectra from shallow angles recorded at different altitudes. The Supplement further discusses SCD<sub>REF</sub> in the case of IO.

Glyoxal dSCDs were derived using a reference spectrum in essentially glyoxal-free air. During RF12 we used an EA0 reference spectrum recorded at 14.5 km for final analysis (no significant glyoxal above 10.5 km). During RF17 we used an EA + 10 reference spectrum at 10.9 km. At this altitude the sky is still sufficiently bright such that the analysis of EA0 spectra at different altitudes is not severely impacted by the photon shot noise of such a reference spectrum; the upward-view at altitude has the additional benefit of systematically minimizing SCD<sub>REF</sub> for glyoxal.

NO<sub>2</sub> dSCDs were derived using an EA + 90 reference spectrum recorded in the MBL during both flights. For H<sub>2</sub>O and O<sub>4</sub>, a common EA + 10 reference spectrum recorded near ceiling altitude were used for final dSCD analysis to minimize SCD<sub>REF</sub> (Table 2, and Sect. 2.8).

Figure 2 shows spectral proof for the detection of BrO, IO and glyoxal. The spectra correspond to BrO, IO and glyoxal dSCDs and RMS noise values as follows: for BrO, dSCD =  $14 \pm 1.8 \times 10^{13}$  molec cm<sup>-2</sup>, RMS =  $3.04 \times 10^{-4}$ ; for IO, dSCD =  $1.8 \pm 0.3 \times 10^{13}$  molec cm<sup>-2</sup>, RMS =  $2.08 \times 10^{-4}$ ; for glyoxal, dSCD =  $8.8 \pm 1.4 \times 10^{14}$  molec cm<sup>-2</sup>, RMS =  $1.91 \times 10^{-4}$ . The fit uncertainty is indicated by the dSCD error.

### 2.8 Profile retrieval from AMAX and SMAX-DOAS

Concentration profiles of trace gases were retrieved using an Optimal Estimation linear inversion (Rodgers, 2000). We use the McArtim (Deutschmann et al., 2011) radiative transfer model (RTM) to interpret the MAX-DOAS measurements. McArtim is a fully spherical Monte Carlo RTM. The radiation fields were constrained by aircraft in situ pressure, temperature and water vapor measurements as well as by CU AMAX-DOAS observations of O<sub>4</sub> at 360 and 477 nm (aerosol extinction). The inference of aerosol extinction profiles from O<sub>4</sub> exploits the fact that the O<sub>4</sub> vertical profile scales with the square of the O<sub>2</sub> concentration and thus only depends on local pressure temperature and water vapor concentrations (Thalman and Volkamer, 2013; Spinei et

**Table 1.** AMAX/SMAX-DOAS analysis settings.

Cross section <sup>a</sup>	Wavelength window (nm)						
	IO 417.5–438	CHOCHO 434.5–460/ 434–460	BrO 340–359	H <sub>2</sub> O 438–458	NO <sub>2</sub> <sup>c</sup> 434.5–460	O <sub>4</sub> (360 nm) 350–387.5 <sup>d</sup>	O <sub>4</sub> (477 nm) 445–485
IO 298 K (1)	x						
CHOCHO 296 K (2)		x			x		
BrO 228 K (3)			x			x	
H <sub>2</sub> O 296 K (4)	x	x		x	x		x
H <sub>2</sub> O 220 K (4)				x			
H <sub>2</sub> O lab. <sup>b</sup>							x
NO <sub>2</sub> 220 K (5)	x/–	x/–	x	x	x	x	x
NO <sub>2</sub> 294 K (5)	–/x	–/x			x		
O <sub>4</sub> 293 K (6)	x	x	x	x	x	x	x
O <sub>4</sub> 203 K (6)							x
HCHO 298 K (7)			x			x	
O <sub>3</sub> 223 K (8)	x/–	x/–	x	x	x	x	x
O <sub>3</sub> 243 K (8)	–/x	–/x				x	
Ring1 250 K (10)	x	x	x	x	x	x	x
Ring2 220 K (9)	x/–	x/–	x	x	x	x	x
Raman (11)	x/–					x	
Residual (12)	–/x	x			x		
Polyn. order	5/3	5/3	5	4	5	5	5

<sup>a</sup> References: (1) Spietz et al. (2005); (2) Volkamer et al. (2005b); (3) Wilmouth et al. (1999); (4) Rothman et al. (2010); (5) Vandaele et al. (1998); (6) Thalman and Volkamer (2013); (7) Meller and Moortgat (2000); (8) Bogumil et al. (2003); (9) Kraus (2006); (10) Gomer et al. (1993); (11) Langford et al. (2007); (12) difference between H<sub>2</sub>O lines in HITEMP and an atmospheric H<sub>2</sub>O reference (Sinreich et al., 2010), see Sect. 3.2.2, Fig. S2 in the Supplement. “/” refers to AMAX/SMAX settings; “x” means the cross section was included, while “–” means it is not included. No distinction means that the same settings were used during the AMAX/SMAX analysis. <sup>b</sup> Cross section recorded with AMAX-DOAS instrument at room temperature through an LED cavity system in the laboratory. <sup>c</sup> NO<sub>2</sub> cross sections at 220 and 296 K where fitted separately and subsequently added while weighted by ambient temperature. <sup>d</sup> Analysis window includes a gap from 366 to 374.5 nm

al., 2015). We use the same aerosol extinction profiles for the inversion of AMAX-DOAS and SMAX-DOAS data during RF17. As input to the inversion, we use tropospheric SCDs for AMAX data as calculated from Eq. (1).

$$\text{SCD} = \text{dSCD} + \text{SCD}_{\text{REF}} \quad (1)$$

For the AMAX-DOAS data the values of SCD<sub>REF</sub> were actively minimized. SCD<sub>REF</sub> is usually unknown for MAX-DOAS retrievals, and – in absence of independent measurements to constrain SCD<sub>REF</sub> – the current state-of-the-art practice with ground-based MAX-DOAS applications is to use dSCDs as input to the inversion (Friess et al., 2006; Clémer et al., 2010; Irie et al., 2011; Wagner et al., 2011; Franco et al., 2015). Knowledge of SCD<sub>REF</sub> facilitates a more direct comparison with RTM but requires independent information. The values of SCD<sub>REF</sub> during RF12 and RF17 are listed in Table 3 and compared with typical dSCD fit errors ( $\Delta\text{dSCD}$ , EA0 spectra at 8 km). SCD<sub>REF</sub> values for NO<sub>2</sub>, H<sub>2</sub>O and O<sub>4</sub> were estimated from RTM initialized for the reference geometry using Real-time Air Quality Modeling System (RAQMS) NO<sub>2</sub>, in situ measurements of temperature/pressure and VCSEL-H<sub>2</sub>O at aircraft altitude and RAQMS profiles at higher altitudes. For BrO, NO<sub>2</sub> and H<sub>2</sub>O the values of SCD<sub>REF</sub> correspond to tropospheric SCDs for

the preferred reference geometry (Table 2). For IO, SCD<sub>REF</sub> was estimated from sensitivity studies to assure accurate correction of the stratosphere (Supplement). For glyoxal, no significant glyoxal was detected when comparing the EA + 10 reference from RF17 with the EA0 reference from 14.5 km (RF12), which further supports that SCD<sub>REF</sub> is essentially 0. Table 3 shows that for BrO, IO and glyoxal the fit error is larger than SCD<sub>REF</sub>, and the measured dSCDs can be approximated as de facto tropospheric SCDs. For NO<sub>2</sub> the value of SCD<sub>REF</sub> is comparable to the fit error, and for H<sub>2</sub>O and O<sub>4</sub> it exceeds the fit error. The effect of uncertain SCD<sub>REF</sub> is largest for SMAX-DOAS profiles and plays a negligible role for measurements near instrument altitude; this is assessed in form of a sensitivity study in Sect. 3.4.

Our retrievals are intended for the troposphere only, i.e., stratospheric absorbers are corrected using nearby reference spectra (Table 2); the successful stratospheric correction is demonstrated (see Sects. 3.2.2 and 4.2). Furthermore, we use an equidistant tropospheric inversion grid that extends to 2–3 km above aircraft ceiling altitude (RF17: 0.5 km layer thickness, 0–13.5 km altitude, RF12: 1, 0–16.5 km). There is at least one, and up to three, independent measurement within each layer to constrain the inversion. A finer grid (0.2 km layer thickness) from 0 to 10 km is used for the in-

**Table 2.** Profile and DOAS reference details.

Flight number/ Ship cruise Date	Profile Time (UTC) Location, SZA (degrees)	Reference spectrum					
		Trace gas	Time (UTC)	Location (degrees)	Altitude (km)	EA (degrees)	SZA (degrees)
RF12 13 Feb 2012	18:54–19:32	BrO	19:28	9.0° N/97.7° W	0.1	0	24.6
	8.6° N/101.2° W	BrO <sup>a</sup>	18:53	8.6° N/101.2° W	14.5	–10	21.7
	9.1° N/97.4° W	BrO <sup>a</sup>	19:31	9.1° N/97.4° W	0.1	+90	25.0
	21.7–25.1	IO <sup>b</sup>	18:48	8.5° N/101.8° W	14.5	0	21.7
		CHOCHO	18:48	8.5° N/101.8° W	14.5	0	21.7
		NO <sub>2</sub>	19:31	9.1° N/97.4° W	0.1	+90	25.0
		H <sub>2</sub> O/O <sub>4</sub>	18:50	8.6° N/101.5° W	14.5	+10	21.7
RF17 26 Feb 2012	15:30–16:48	BrO	15:30	5.9° N/91.8° W	0.1	0	44.8
	5.9N/91.8W	IO <sup>a</sup>	16:57	7.2° N/89.5° W	10.9	+10	24.4
	6.7° N/90.5° W	IO <sup>a</sup>	16:53	7.0° N/90.0° W	10.9	–10	25.5
	44.8–26.6	IO <sup>a</sup>	15:25	6.1° N/91.6° W	0.1	0	45.9
		CHOCHO	16:50	6.8° N/90.3° W	10.9	+10	26.0
		CHOCHO <sup>a</sup>	16:53	7.0° N/90.0° W	10.9	–10	25.5
	CHOCHO <sup>a</sup>	15:25	6.1° N/91.6° W	0.1	0	45.9	
	NO <sub>2</sub>	15:29	5.9° N/91.8° W	0.1	+90	44.8	
	H <sub>2</sub> O/O <sub>4</sub>	16:57	7.2° N/89.5° W	10.9	+10	24.4	
KA-12-01 26 Feb 2012	15:53–15:58						
	5.85° N/91.99° W						
	– 5.84° N/91.97° W 39.6–38.3	IO/CHOCHO	15:52	5.54° N/91.97° W	0.01	+90 <sup>c</sup>	38.3

<sup>a</sup> References used for sensitivity studies shown in Figs. 5 and 6. <sup>b</sup> Spectrum used to evaluate RF12 and RF17 to minimize IO contained in reference. <sup>c</sup> Nearest zenith spectrum used to analyze one SMAX-DOAS off-axis EA scan (+0.8, +1.5, +3.8, +10.0, +25.0).

**Table 3.** AMAX SCD<sub>REF</sub> values and fit uncertainties.

Trace gas	SCD <sub>REF</sub> (molec cm <sup>–2</sup> )		Typical ΔdSCD*	Estimated from
	RF12	RF17		
BrO	1 × 10 <sup>13</sup>	1 × 10 <sup>13</sup>	1.3 × 10 <sup>13</sup>	Sensitivity studies (see 3.2.1, 3.2.2 and Supplement)
IO	0.6 × 10 <sup>12</sup>	0.6 × 10 <sup>12</sup>	2.1 × 10 <sup>12</sup>	Sensitivity studies (see 3.2.1. and Supplement)
CHOCHO	0	0	1.3 × 10 <sup>14</sup>	RF17 EA + 10 reference
NO <sub>2</sub>	0.42 × 10 <sup>15</sup>	0.92 × 10 <sup>15</sup>	0.13 × 10 <sup>15</sup>	RAQMS NO <sub>2</sub>
H <sub>2</sub> O	0.81 × 10 <sup>23</sup>	0.98 × 10 <sup>23</sup>	1.8 × 10 <sup>21</sup>	VCSEL H <sub>2</sub> O
O <sub>4</sub> , 360 nm	(0.83 ± 0.25) × 10 <sup>43</sup> molec <sup>2</sup> cm <sup>–5</sup>	(1.50 ± 0.25) × 10 <sup>43</sup> molec <sup>2</sup> cm <sup>–5</sup>	2.9 × 10 <sup>41</sup> molec <sup>2</sup> cm <sup>–5</sup>	In situ <i>T</i> , <i>p</i> , H <sub>2</sub> O; RAQMS <i>p</i> and MTP <i>T</i> above
O <sub>4</sub> , 477 nm	(1.05 ± 0.20) × 10 <sup>43</sup> molec <sup>2</sup> cm <sup>–5</sup>	(1.28 ± 0.20) × 10 <sup>43</sup> molec <sup>2</sup> cm <sup>–5</sup>	0.9 × 10 <sup>41</sup> molec <sup>2</sup> cm <sup>–5</sup>	In situ <i>T</i> , <i>p</i> , H <sub>2</sub> O; RAQMS <i>p</i> and MTP <i>T</i> above

\* For EA 0 spectrum at ~ 8 km.



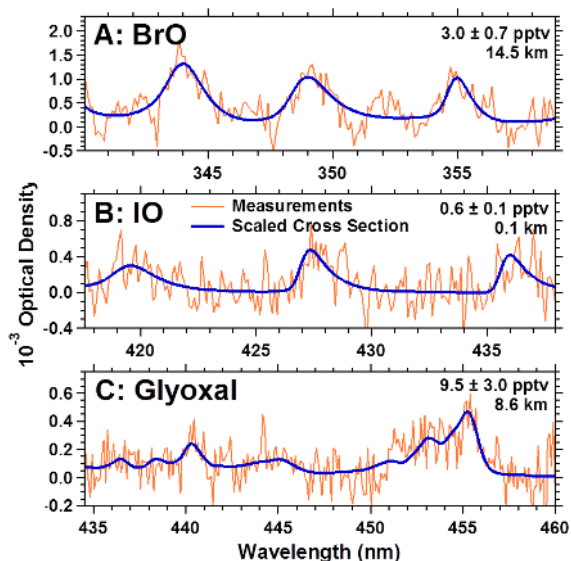


**Figure 2.** Spectral proof of the detection of BrO, IO and glyoxal. Fitted cross sections are overlaid on measured signal including the noise level of the instrument. All spectra are recorded with EA0. Date, time, location, altitude and solar geometry are as follows. BrO(RF12): 14 February 2012, 18:54 UT, 101.2° W/8.7° N, 14.5 km, 21.7° SZA; IO(RF17): 26 February 2012, 15:28 UT, 91.7° W/5.9° N, 0.1 km, 45.1° SZA; glyoxal (RF12): 14 February 2012, 19:01 UT, 100.2° W/8.7° N, 8.6 km, 21.8° SZA.

version of the SMAX-DOAS data. Figure S1 shows all the a priori profiles of trace gases used in the AMAX and SMAX-DOAS inversions. The measurement error covariance matrix was constructed using the square of the DOAS fit error as the diagonal elements of the matrix and setting all non-diagonal elements to 0. The a priori error covariance matrix contains the a priori error as diagonal elements. For the AMAX retrievals the a priori error was set to 10 000 % to provide maximum freedom for the retrievals (typically well constrained by the measurements over all altitudes). SMAX retrievals used a 100 % a priori error. Minimal smoothing was applied by setting the correlation height that determines the non-diagonal elements in the a priori error covariance matrix equal to the inversion grid height for both AMAX and SMAX inversions.

Aerosols are represented in the RTM as described in Table 4. The aerosol extinction profiles were obtained using the iterative forward model approach described in detail in (Baidar et al., 2013a). Briefly, a set of measured  $O_4$  SCDs is related to the aerosol extinction vertical profile using a forward RTM calculation. The predicted  $O_4$  SCDs are then compared with the measured  $O_4$  SCDs, and the aerosol extinction profile is varied iteratively using an onion peeling from top to surface until the predicted and measured  $O_4$  SCDs agree (see Baidar et al. (2013a) for details). The  $O_4$  box air mass factors (Box-AMF) closely resemble those shown in Fig. S2, i.e., the  $O_4$  measurement is almost entirely sensitive at measurement altitude, and nearly all of the ver-

tical information contained in the SCD comes from that particular altitude. Aerosol extinction at other wavelengths was linearly interpolated between 360 and 477 nm to the wavelength used in the inversion (Table 4).

Box-AMFs are a measure of the instrument sensitivity and characterize the ratio of the partial SCD to the partial vertical column density (VCD) within one atmospheric layer (defined by the vertical grid resolution of the RTM). Box-AMFs are included for both AMAX-DOAS profile case studies at the wavelengths used for the BrO (350 nm), IO (428 nm) and glyoxal (447 nm) profile retrievals in Fig. S2. The inversion errors are typically dominated by the measurement noise and are given by the retrieval noise covariance matrix. For a discussion on the error budget of the optimal estimation inversion, including the propagation of errors caused by smoothing, choice of a priori and extinction errors through the Optimal Estimation retrieval, see Baidar et al. (2013a).

## 2.9 Real-time Air Quality Modeling System model

Chemical and meteorological forecasts from the RAQMS (Pierce et al., 2007) in conjunction with reverse domain filling (RDF) techniques (Sutton et al., 1994) are used to provide information on air mass histories for the TORERO flights. RAQMS is a unified (stratospheric and tropospheric) air quality modeling/data assimilation system with online chemistry. RAQMS has a horizontal resolution of  $1 \times 1^\circ$  with 35 hybrid eta–theta vertical levels extending from the surface to approximately 60 km. RAQMS chemistry includes  $O_x$ – $HO_x$ – $NO_x$ – $ClO_x$ – $BrO_x$  cycles governing the formation and destruction of odd oxygen, tropospheric  $NO_x$ – $HO_x$  reactions, oxidation of  $CH_4$  and CO following Pierce et al. (2003, 2007) and inclusion of non-methane hydrocarbon (NMHC) chemistry following Zaveri and Peters (1999). The RAQMS online chemistry module is originally based on the LaRC Interactive Modeling Project for Atmospheric Chemistry and Transport (IMPACT) model (Eckman et al., 1995) and uses a family approach to predict total odd oxygen, total odd nitrogen and total inorganic chlorine and bromine.  $HO_x$  is assumed to be in photochemical equilibrium. Species such as NO, which is not explicitly transported, are solved by partitioning total odd nitrogen assuming photochemical equilibrium. The family approach allows for longer chemical time steps and minimizes the computational cost of the RAQMS chemistry. This is particularly important since RAQMS is used to provide real-time global chemical and aerosol analyses and forecasts. The RAQMS aerosol prediction uses online aerosol modules from GOCART (Chin et al., 2002, 2003) as discussed in Verma et al. (2009). RAQMS chemical analyses include assimilation of cloud-cleared total column ozone from the Ozone Monitoring Instrument (OMI) and stratospheric ozone profiles from the Microwave Limb Sounder on the NASA Aura satellite. RAQMS aerosol analyses include assimilation of aerosol optical depth from the



**Table 4.** AMAX/SMAX RTM parameters.

Parameter	Values used in RTM	
Wavelength [nm]	350 (BrO), 360, 477 (O <sub>4</sub> ), 428/428 (IO), 447/455 (CHOCHO), 447 (NO <sub>2</sub> , H <sub>2</sub> O)	
Field of view	0.17°/0.3°	
Atmosphere	In situ data: <i>p</i> , <i>T</i> , O <sub>4</sub> , O <sub>3</sub> , H <sub>2</sub> O; model data: NO <sub>2</sub> and <i>p</i> , <i>T</i> , O <sub>4</sub> , O <sub>3</sub> above max. aircraft altitude	
Surface albedo	350, 360 nm: 0.05; 428–477 nm: 0.08/0.1	
Aerosol	RF12	RF17/ship
AOD (428 nm)	0.35	0.41
G-parameter	0.75 (0–2 km), 0.72 (2 km TOA)	0.75 (0–2 km), 0.72 (2 km TOA)/0.74
SSA*	0.97 (< 400 nm), 0.98 (> 400 nm)	0.97 (< 400 nm), 0.98 (> 400 nm)

\* SSA is single scattering albedo.

Moderate Resolution Imaging Spectroradiometer (MODIS) on the NASA Terra and Aqua Satellites.

Meteorological forecasts are initialized with operational analyses from the National Centers for Environmental Prediction Global Data Assimilation System. Six-hour chemical and meteorological forecasts provide chemical and meteorological input for the RDF calculations. The RAQMS RDF calculations are based on analysis of back trajectories initialized along the aircraft flight track. Three-dimensional 7-day back-trajectory calculations were conducted using the Langley trajectory model (Pierce and Fairlie, 1993) and initialized at model hybrid levels every 5 min along the TORERO flight tracks.

### 2.10 Atmospheric state during the RF12 and RF17 case studies

RF12 was conducted on 14 February 2012, and RF17 took place on 26 February 2012. Both flights were from/to San Jose, Costa Rica, and headed west over the northern hemispheric tEPO to probe mostly cloud-free air. Times and locations of the two profile case studies are given in Table 2. Both profiles probed pristine marine air below 2 km and did not show signs of land influences inside the MBL, as indicated by chemical tracer measurements of hydrocarbons by the Trace Organic Gas Analyzer (Apel et al., 2003, 2010) on the aircraft (not shown) and back-trajectory calculations by the RAQMS model. The MBL-CO below 2 km was 80–98 ppbv (RF12) and 96–109 ppbv (RF17). Above 8 km, measurements of CO ranged between 40 and 60 ppbv and of NO<sub>2</sub> were near 10 pptv, indicating mostly aged FT air. Some minor pollution influences were observed between 2 and 8 km (~25 pptv NO<sub>2</sub>, both flights). Analysis of 7-day back trajectories and tracer measurements on board consistently showed that the air above ~10 km (RF12) and above 8 km (RF17) had spent more than 85 % of the time in the upper FT. RF12 trajectories further showed influences from tropical deep convection up to 11 km which were generally more prominent in the lower and mid-FT. During RF17 deep convection influences were more recent, stronger below 5–6 km

and weaker but nonzero over the full altitude range probed. Neither case study showed evidence for stratospheric influences over 7 days. RAQMS consistently showed the thermal tropopause at ~16–17 km, in good agreement with Microwave Temperature Profiler (MTP) measurements (Denning et al., 1989; Lim et al., 2013) aboard the aircraft (not shown).

## 3 Results

### 3.1 Aerosols and clouds

The aerosol extinction profile shown in Fig. 3 was derived using O<sub>4</sub> data from the EA0 measured at 477 nm during the RF17 ascent above the ship. To get a sense of the error in AMAX extinction profiles, two additional extinction profiles were retrieved for each set of measured O<sub>4</sub> SCDs: one profile matched the positive error bars of the measured O<sub>4</sub> SCDs and another matched the negative error bars. The O<sub>4</sub> error bars are defined as the sum of the SCD<sub>REF</sub> uncertainty and the DOAS fit error. The SCD<sub>REF</sub> was determined explicitly through RTM calculations (Sect. 2.8), and the uncertainty in SCD<sub>REF</sub> was estimated from trying to match a complete measured angle scan (EA 0, +1, +2, +5, +10) in a nearly pure Rayleigh atmosphere. We estimate an SCD<sub>REF</sub> uncertainty of  $2.5 \times 10^{42}$  molec<sup>2</sup> cm<sup>-5</sup> and  $2.0 \times 10^{42}$  molec<sup>2</sup> cm<sup>-5</sup> at 360 and 477 nm. These error bars are about 10–20 times higher than the O<sub>4</sub> fit error (Sect. 2.8) and estimated conservatively. The comparison with Mie calculations in Fig. 3 show that particularly at 477 nm these numbers can be taken as upper limits. The resulting extinction error bars are shown as red background to the AMAX extinction in Fig. 3.

The O<sub>4,477</sub> inferred aerosol extinction,  $\epsilon_{477}$ , is compared with the HSRL<sub>477</sub> extinction and Mie calculations of UHSAS size distributions in Fig. 3. The  $\epsilon_{477}$  was 0.104 km<sup>-1</sup> in the lower 400 m, which compared within 6 % with the average HSRL<sub>477</sub> extinction of  $0.098 \pm 0.013$  (i.e., 0.085 km<sup>-1</sup> and 0.11 km<sup>-1</sup>, respectively). Under these conditions the av-

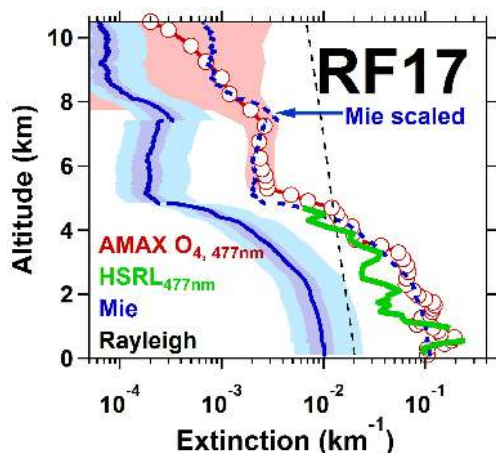


**Figure 3.** Comparison of aerosol extinction inferred from AMAX- $O_4$  measured at 477 nm and Mie calculations constrained by aerosol size distribution measurements on the GV. The blue and red shading indicates the uncertainties in the Mie and  $O_4$ -inferred extinction. See Sects. 2.1.3, 2.2 and 3.1 for details.

erage deviations ( $[O_{4, \text{meas}} - O_{4, \text{RTM}}]/O_{4, \text{RTM}}$ ) between measured and predicted  $O_4$  SCDs were  $1 \pm 2\%$  (Fig. 4).

By comparison, the Mie calculations consistently find lower extinction. The extinction inside the boundary layer was lower than that due to Rayleigh scattering and a factor of  $\sim 10.8$  lower compared to that measured by HSRL and AMAX-DOAS. The reason for this difference is currently not clear. Models indicate evaporation of water from the particles prior to sizing could cause a factor of two reduction in extinction (light blue shading in Fig. 3). Also, discrepancies between the index of refraction for PSL (polystyrene latex) spheres used for UHSAS calibration and actual aerosol index of refraction may result in undersizing of larger particles. However, without knowing the actual aerosol index of refraction, it is difficult to assess the impact of this index contrast. The solid line corresponds to the average value of extinction, and the dark blue shading indicates the variability for different values of  $n$  (see Sect. 2.2). We have performed RTM calculations that used  $HSRL_{477}$  and UHSAS extinction profiles instead of  $\epsilon_{477}$  to predict  $O_{4, \text{RTM}}$ . The results are shown in Fig. S4 and confirm that sub-Rayleigh aerosol extinction results in  $O_{4, \text{RTM}}$  that is considerably larger than measured. One possibility for the difference could be the presence of few larger particles that may not be measured by UHSAS. In this context it is surprising that the UHSAS extinction profile shape closely resembles the  $O_4$ -inferred profile shape by applying a constant factor at all altitudes. The renormalized UHSAS profile (here multiplied by 10.8) closely resembles also at the very low  $\epsilon_{477}$  values in the free troposphere.

To our knowledge the only assessment of the accuracy of  $O_4$  SCDs in the presence of aerosols is that by (Thalman and Volkamer, 2010). That study employed monodisperse PSL spheres of known size under controlled con-

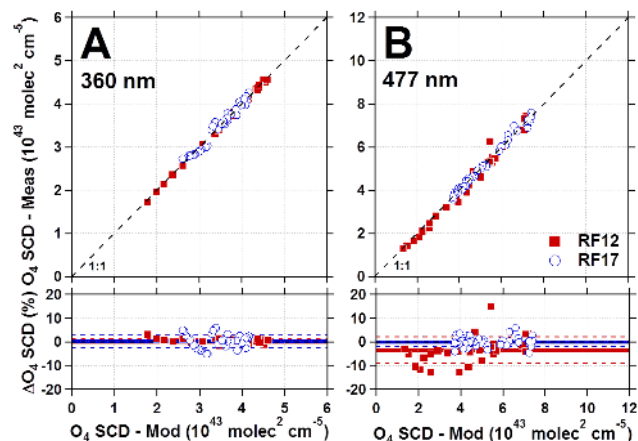


**Figure 4.** Comparison of measured and predicted  $O_4$  SCDs for the two profile case studies. The lower panels show the relative difference to the 1 : 1 line; solid lines represent the median bias and dashed lines the  $1\sigma$  standard deviation of scatter around the 1 : 1 line.

ditions in the laboratory and found excellent agreement between  $O_4$ -inferred and Mie calculated extinction (see their Fig. 8). These results extend upon previous assessments that  $O_4$  measurements by CU AMAX-DOAS agree with direct-sun DOAS and RTM predictions in a Rayleigh atmosphere (agreement better 5%) (Spinei et al., 2015; Thalman et al., 2014). The measured and predicted  $O_4$  SCDs are compared for RF12 and RF17 in Fig. 4. For both case studies the agreement is excellent ( $R^2 > 0.96$ ), with slopes of unity within error and insignificant intercepts at both wavelengths ( $< 1.4 \times 10^{42} \text{ molec}^2 \text{ cm}^{-5}$  at 360 nm, and  $< 2.8 \times 10^{42} \text{ molec}^2 \text{ cm}^{-5}$  at 477 nm). There is furthermore no obvious trend in the deviations. In particular, the lack of a significant offset in Fig. 4 indicates the absence of obvious limitations from cloud effects and reasonable knowledge of  $SCD_{\text{REF}}$ . We have investigated the effect of clouds for RF17, where scattered clouds were visible from the aircraft to the south of the ship. A simulated cloud with optical depth 15 between 0.4 and 1.1 km increased the predicted  $O_4$  SCD at EA0 at 2 km by  $+3 \times 10^{42} \text{ molec}^2 \text{ cm}^{-5}$  and by  $+10 \times 10^{42} \text{ molec}^2 \text{ cm}^{-5}$  at 10 km (both wavelengths). For comparison, this is up to 13 times larger than the intercepts in Fig. 4 (RF17, 360 nm:  $1.4 \pm 1.0 \times 10^{42} \text{ molec}^2 \text{ cm}^{-5}$ ; 477 nm:  $-0.02 \pm 0.79 \times 10^{42} \text{ molec}^2 \text{ cm}^{-5}$ ) and 4 times larger than the uncertainty in  $SCD_{\text{REF}}$ . We can thus rule out significant cloud influences on RTM during our RF17 case study; RF12 was conducted in mostly cloud-free air.

The  $O_4$ -inferred extinction profiles integrated over altitude correspond to aerosol optical depth at 477 and 360 nm of  $0.37 \pm 0.04$  ( $HSRL_{477}$ : 0.27) and  $0.53 \pm 0.26$  for RF17, and  $0.32 \pm 0.07$  and  $0.31 \pm 0.22$  for RF12. The  $O_4$  band at 477 nm is better suited to infer aerosol extinction than the 360 nm  $O_4$  band because of the larger  $O_4$  cross section at 477 nm, larger  $O_4$  dSCDs (i.e., 3.1 times longer photon paths

in Rayleigh conditions) and more abundant photons (and thus smaller dSCD fit error); also if clouds are present the effect on  $O_4$  is expected to be relatively smaller due to the larger  $O_4$  dSCD at 477 nm. Reasonable error bars are only obtained using the  $O_4$  band at 477 nm. At 360 nm aerosol extinction measurements are less precise, and aerosol extinction is partially masked by the stronger Rayleigh scattering at ultraviolet wavelengths. Such masking in principle also makes trace-gas retrievals at ultraviolet wavelengths (e.g., BrO, formaldehyde) less dependent on a priori knowledge about aerosol extinction. A previous radiation closure study using aircraft integrated extinction from in situ size distributions and compared it with a sun photometer at 525 nm. The differences were largest (up to 41 %) at low aerosol loadings in the upper FT (Collins et al., 2000). In this work the minimum aerosol extinction was observed during RF12 at 10 km ( $\sim 2.8 \times 10^{-4} \text{ km}^{-1}$ , factor of 25 sub-Rayleigh). Extinction measurements using  $O_4$  at 477 nm have potential to inform future radiation closure studies in environments characterized by low aerosol extinction.

### 3.2 Uncertainties and sensitivity studies of dSCDs

The CU AMAX-DOAS instrument provides flexible choice of geometry to record reference spectra. This flexibility is used here to assess the robustness of trace-gas dSCDs by comparing results from reference spectra of different geometries. The final reference spectrum is optimized to minimize  $SCD_{REF}$ , thereby maximizing sensitivity (Sect. 2.8), and to accurately cancel out stratospheric contributions of  $NO_2$  and BrO. Details about all reference spectra tested are included in Table 2. In the following we focus on robustness of dSCDs for weak absorbers like BrO, IO and glyoxal – measurements of the stronger absorbers  $NO_2$ ,  $H_2O$  and  $O_4$  follow the same rationale (Tables 1, 2) and are more routine (see e.g., Baidar et al., 2013a).

#### 3.2.1 References

##### BrO

Figure 5a shows the Box-AMFs for three reference geometries that we have tested for BrO: MBL EA + 90, MBL EA0 and EA – 10 from ceiling altitude. The limb–zenith comparison is most sensitive for detecting any BrO in the MBL; all three references assure proper stratospheric correction for BrO (see Sects. 3.2.2 and 4.2, Fig. 5a), and MBL references have lower  $SCD_{REF}$ . EA – 10 at altitude is chosen to test for the intrinsic offset consistency between BrO dSCDs. A zenith spectrum at altitude – while desirable – is not practical, because the low photon count does not facilitate sufficiently good signal to noise for BrO analysis. Figure 5c compares the retrieved BrO dSCDs. For RF12 we find slopes of unity and very strong correlations ( $R^2 \geq 0.99$ ). The offset of BrO dSCDs was compared with those expected

based on RTM forward calculations that represented our retrieved BrO inversion profiles. For example, for RF12 we find that the offsets for correlations of dSCDs of MBL EA0 and EA – 10 at altitude ( $-7.2 \pm 0.5 \times 10^{13} \text{ molec cm}^{-2}$ ) and MBL EA + 90 ( $0.1 \pm 0.6 \times 10^{13} \text{ molec cm}^{-2}$ ) are consistent with that expected from our profiles ( $-5.6 \pm 1.2 \times 10^{13}$  and  $0.3 \pm 0.1 \times 10^{13} \text{ molec cm}^{-2}$ ). A similar agreement is also observed for RF17. The limb spectra provide a particularly stable analysis, facilitate RMS that closely resembles photon shot noise and do not depend on altitude (see Fig. 5b); using the zenith spectra gives generally consistent results but introduces some scatter (variations of  $\sim 2 \times 10^{13} \text{ molec cm}^{-2}$  BrO dSCD) that is seen neither when using the limb reference nor when using the EA – 10 reference.

##### Glyoxal

The Box-AMFs for four reference geometries are shown in Fig. 6A and correspond to geometry MBL EA0 and EA – 10, EA + 10 and EA0 (all at 10.9 km). EA + 10 is chosen to minimize  $SCD_{REF}$  during RF17 (EA0 at altitude can also be used if taken in glyoxal-free air, like RF12, Table 2).  $SCD_{REF}$  is minimized during both case studies, which maximizes the signal-to-noise ratio for glyoxal detection in limb spectra at any other altitude (Fig. 6b). All references assure proper stratospheric correction (no glyoxal expected based on our data), but here we go one step further. The different Box-AMFs test the robustness of glyoxal dSCDs with respect to the presence or absence of  $NO_2$  (e.g., comparing EA – 10 and EA + 10 at altitude) and provide a consistency check of our profiles (e.g., comparing MBL EA0 with EA + 10 at altitude). Figure 6d compares these glyoxal dSCDs for RF17 (the EA + 10 reference at altitude is plotted on the  $x$  axis; see Sect. 2.6 “Reference spectra and trace-gas dSCDs”, Table 2). We find slopes of unity and very strong correlations ( $R^2 \geq 0.94$ ). The offsets for EA – 10 ( $-6.7 \pm 0.1 \times 10^{14} \text{ molec cm}^{-2}$ ) and EA0 ( $-1.46 \pm 0.05 \times 10^{15} \text{ molec cm}^{-2}$ ) are consistent with those expected from our profiles ( $-7 \pm 3 \times 10^{14}$  and  $1.3 \pm 0.4 \times 10^{15} \text{ molec cm}^{-2}$ ). Similar agreement is also observed for RF12. The EA + 10 at altitude provides a stable analysis, facilitates RMS that closely resembles photon shot noise and does not depend on altitude (see Fig. 6b).

##### IO

The offsets for IO dSCDs are compared for RF17 in Fig. 6c. The RF12 EA0 reference at ceiling altitude is used to derive dSCDs plotted on the  $x$  axis (see Sect. 2.6, Table 2). The slopes differ by less than 10 % from unity, and correlations are very strong ( $R^2 \geq 0.94$ ). The offsets for RF17 reference EA – 10 at altitude ( $-7.9 \pm 0.2 \times 10^{12} \text{ molec cm}^{-2}$ ) and RF17 MBL EA0 ( $-17.2 \pm 0.02 \times 10^{12} \text{ molec cm}^{-2}$ ) are in very close agreement with those expected from our profiles ( $-8 \pm 4 \times 10^{12}$  and  $-16 \pm 5 \times 10^{12} \text{ molec cm}^{-2}$ ). Sim-

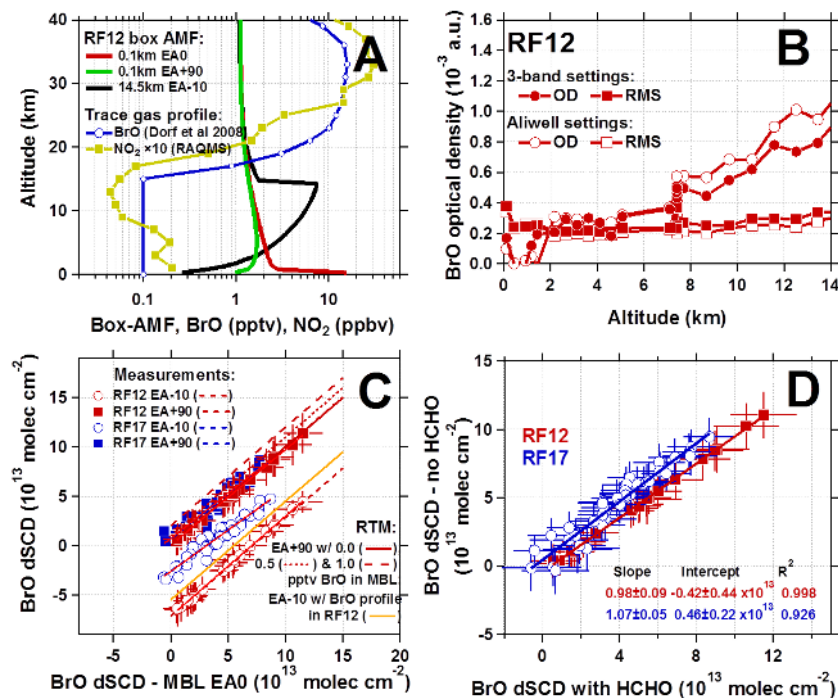


**Figure 5.** Assessment of the robustness of BrO dSCDs. (a) Box-AMFs for different geometries of reference spectra used during spectral fitting to derive dSCDs; a generic profile for BrO in the tropics and the NO<sub>2</sub> profile from the RF12 case study are also shown for comparison. (b) Signal-to-noise ratio for BrO detection as a function of altitude and comparison of the three-band BrO analysis window with fit settings of the two-band analysis of Aliwell et al. (2002). (c) Consistency of the intrinsic offset between dSCDs with RTM (see Sect. 3.2.1 for details). (d) Insensitivity of BrO dSCDs towards including or excluding a HCHO reference spectrum during analysis.

ilar agreement is also observed for RF12. Notably, the effect of vibrational Raman scattering in the IO wavelength range is small (Coburn et al., 2011) and can be ruled as a potential source of bias for our IO dSCDs. Our reference (Table 2) provides a stable analysis, facilitates RMS that closely resembles photon shot noise and does not depend on altitude (see Fig. 6b). Furthermore, when the IO dSCDs derived from EA + 10 and EA0 at ceiling altitude are compared, there is no significant difference.

### 3.2.2 Further sensitivity studies

#### BrO – quality of stratospheric correction

The tropopause is located 2–3 km above the ceiling altitude of the aircraft, where the Box-AMFs for the limb, zenith and EA – 10 reference spectra have virtually identical sensitivity (Fig. 5a). The stratosphere is characterized equally well from using either of the different references. To further quantify the uncertainty due to stratospheric BrO for tropospheric BrO dSCDs we have simulated stratospheric SCDs (SCD<sub>strat</sub>) for the three reference geometries shown in Fig. 5a and for the EA0 spectra from the aircraft descent. The RTM forward calculations use a RAQMS BrO profile, setting all values below 16.5 km to 0. The simulated SCD<sub>strat</sub> for the references are  $1.09 \times 10^{13}$ ,  $1.09 \times 10^{13}$  and  $1.1 \times 10^{13}$  for

the MBL limb, MBL zenith and EA – 10 at altitude reference spectra, respectively. The mean SCD<sub>strat</sub> of forward-looking spectra that add to the profile (RF12 geometries) is  $1.12 \pm 0.05 \times 10^{13}$  molec cm<sup>-2</sup>. The agreement is within 1σ error, demonstrating that stratospheric contributions cancel out to better than  $0.03 \times 10^{13}$  molec cm<sup>-2</sup> BrO dSCD for all three geometries. This is ~30 times smaller than the measurement error. Similar results are observed also for NO<sub>2</sub> (see Sect. 4.2).

#### BrO dSCD – robustness of fit window and lack of HCHO sensitivity

We further test the robustness of the BrO dSCDs by comparing with the two-band analysis settings (Aliwell et al., 2002) that are widely used for BrO analysis of zenith-sky and direct-sun balloon DOAS. We use a wider BrO fitting window (three-band analysis) in this work, because limb observations do not suffer from strong stratospheric ozone interferences that need to be actively avoided by fitting a smaller BrO window with zenith-sky and direct-sun balloon DOAS (Van Roozendaal et al., 2002), as had previously been noted for satellite and ground-based measurements of tropospheric BrO (Van Roozendaal et al., 2002; Hendrick et al., 2007; Theys et al., 2007). Figure 5b compares the three-band analysis with the two-band analysis and the noise level of the

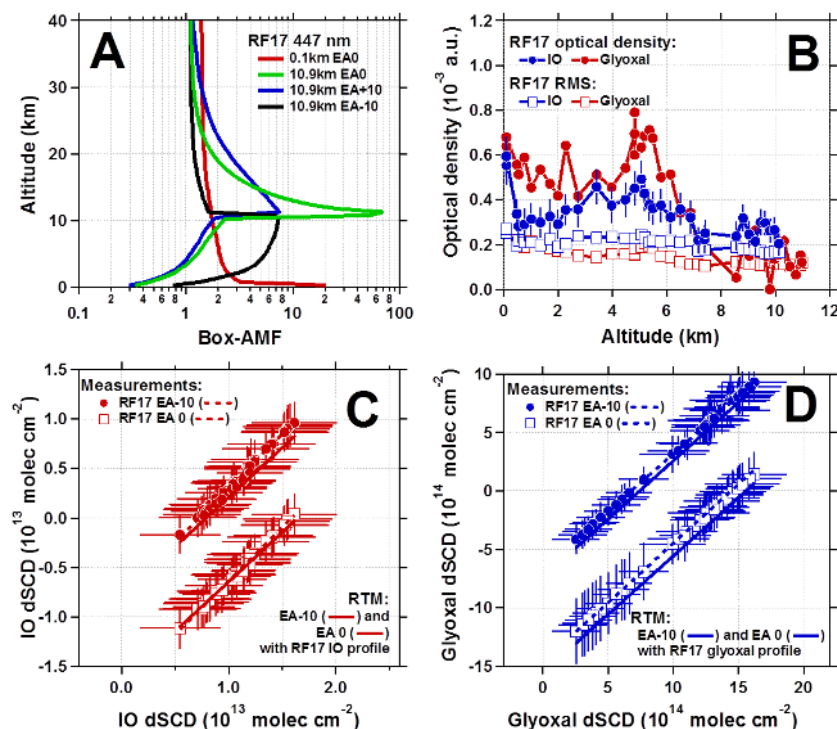


**Figure 6.** Assessment of the robustness of glyoxal and IO dSCDs. (a) Box-AMFs for different geometries of reference spectra. (b) Signal-to-noise ratio for glyoxal (red) and IO (blue) detection as a function of altitude. (c) Consistency for IO and (d) glyoxal of the intrinsic offset among dSCDs with RTM. See Sect. 3.2.1 for details.

instrument as a function of altitude. The BrO dSCD is expressed as optical density (dSCD times absorption cross section) for this purpose. Both analysis settings agree within fit error. There is furthermore no dependence of the RMS noise as a function of altitude with either analysis. The three-band BrO fit window gives slightly smaller optical density but also results in reduced error bars, confirming that BrO is conservatively estimated here. Furthermore, Fig. 5d assesses the robustness of BrO dSCDs towards HCHO cross sensitivities (Vogel et al., 2013). For our three-band analysis, correlations among BrO dSCDs derived from evaluations that differed only in the fact that a HCHO cross section spectrum is included (Table 1) or excluded from the fit show slopes that are unity within 2–7 %. The intercepts are generally smaller than  $0.5 \times 10^{13}$  molec cm<sup>-2</sup>, which is below fit error. No significant sensitivity towards HCHO is observed for the three-band analysis.

The glyoxal and IO dSCDs are robust within the indicated error bounds for variations to the fit window and polynomial order (Supplement). For IO and glyoxal, a comparison of signal-to-noise ratio as a function of altitude is shown in Fig. 6b. There is no altitude dependence in the RMS with either trace gas. The best signal-to-noise ratio is observed for IO in the MBL and for glyoxal in the mid-FT. For both gases the RMS noise closely resembles the photon shot noise that

is expected based on the number of photons collected (see Eq. (2) in Coburn et al., 2011) in our final analysis.

### Sensitivity to H<sub>2</sub>O spectral line parameters

The IO dSCDs showed a slightly larger sensitivity (~ 16 %) than glyoxal dSCDs (~ 10 %) to the choice of H<sub>2</sub>O reference spectra (Fig. S3). This sensitivity is due to missing water lines in spectral databases such as HITEMP and HITRAN. For IO no further action was taken to account for these lines, since no apparent structure was observed in the RMS residual of the IO fit. For glyoxal, the sensitivity in the dSCDs is generally smaller than for IO; it is found to be further reduced when a H<sub>2</sub>O residual spectrum is included in the fit (equivalent to the procedure by Sinreich et al., 2007, 2010). The residuum does not affect the glyoxal dSCDs when it is removed from the fit, i.e., the glyoxal dSCDs changes by ~ 4 % whether the residuum is included or excluded in the fit for either spectral database (Fig. S3). We estimate the uncertainty in the glyoxal dSCDs due to choice of spectral parameters as 10 % in our final analysis. Interestingly, the residuum spectrum has a balancing effect towards choice of spectral database (Fig. S3). Other than this, the effect of the residuum is cosmetic and helps to remove the H<sub>2</sub>O peak at 442 nm that is well separated from the wavelength range with strongest glyoxal absorption at 455 nm. Corroborating evidence comes from measurements of H<sub>2</sub>O reference spec-



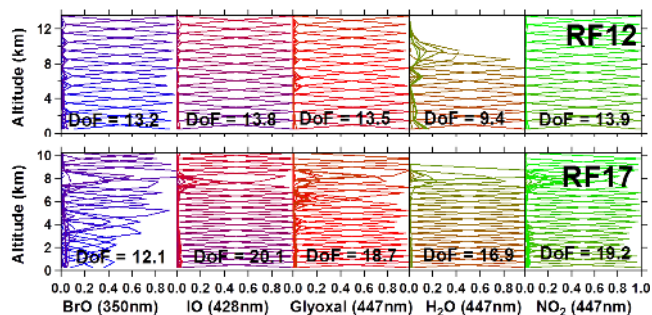


**Figure 7.** Characterization of the AMAX profiles of BrO, IO, glyoxal, H<sub>2</sub>O and NO<sub>2</sub> in terms of AVK and DoF for RF12 and RF17. The larger number of DoF during RF17 is the result of a shorter integration time for limb spectra during the aircraft ascent. See Sects. 2.8 and 3.3.

tra using CE-DOAS (Supplement), intercomparison of CE-DOAS with seven other techniques under simulated atmospheric conditions that systematically varies absolute humidity (Thalman et al., 2015) and field measurements of eddy covariance (EC) fluxes of glyoxal and H<sub>2</sub>O (Coburn et al., 2014), as is discussed further in the Supplement.

In light of the possibility of small IO amounts in the stratosphere (Wennberg et al., 1997; Dix et al., 2013), an assessment of SCD<sub>REF</sub> is included for IO in the Supplement.

### 3.3 Characterizing the AMAX-DOAS trace-gas retrievals

The averaging kernel (AVK) is a product of the optimal estimation inversion. It indicates how the retrieved state is related to measurements and a priori (see also Sect. 3.4 “Sensitivity of MAX-DOAS profiles to SCD<sub>REF</sub>”). Figure 7 shows AVKs that peak at unity, which indicates that our trace-gas profiles retrievals for BrO, IO, glyoxal, H<sub>2</sub>O and NO<sub>2</sub> are well constrained by measurements. An AVK peaks at unity when the information at this altitude comes from the measurement and is independent of the a priori profile assumption. The number of independent concentration points is quantified by the degrees of freedom (DoF). Our limb measurements have 12–13 DoF for tropospheric BrO, 14–20 DoF for IO, 12–17 DoF for glyoxal and 13–20 DoF for NO<sub>2</sub>. This corresponds to about 500 m vertical resolution (RF17) and 1 km vertical resolution for RF12. This difference in resolution is due to longer averaging times for spectra during RF12, which reduces the number of dSCD values that enter the inversion. Measurements at higher time resolution over a higher altitude range have potential to increase DoF for BrO and also IO, glyoxal and NO<sub>2</sub> accordingly.

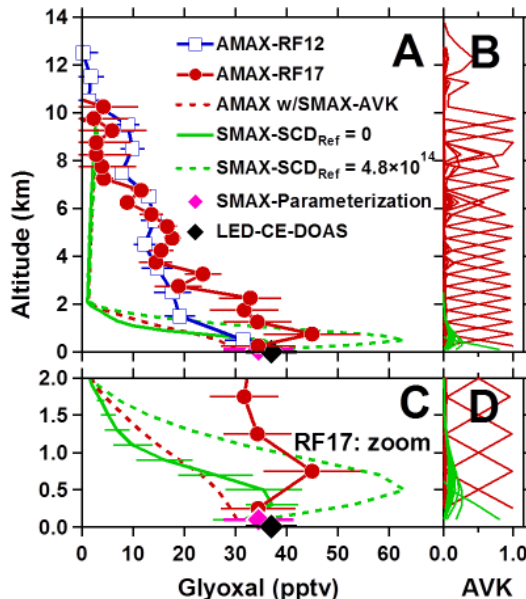


**Figure 8.** Glyoxal vertical profiles and comparison with independent validation data on the ship. (a) AMAX-DOAS during RF12 (blue squares) and RF17 (red dots) is compared with LED-CE-DOAS (black diamond) and SMAX-DOAS parameterization (magenta diamond) and optimal estimation retrievals (green lines); (b) shows AVK for glyoxal from RF17 (red) and SMAX-DOAS (green); (c) is the same as (a) but with only RF17 data and zoomed for the lower 2 km. SMAX profile inversion of dSCDs is the solid green line; SCD<sub>REF</sub> =  $4.8 \times 10^{14}$  molec cm<sup>-2</sup> glyoxal is the dashed green line; simulated SMAX-DOAS view of the AMAX profile using Eq. (2) is the red dashed line; see Sect. 3.4 “Sensitivity of MAX-DOAS profiles to SCD<sub>REF</sub>” for details. (d) is the same as (b), zoomed for the lower 2 km. The error bars are based on propagating fit errors through the inversion.

### 3.4 Characterizing the SMAX-DOAS trace-gas retrievals

Figures 8b, d and 9b, d show in green the AVKs for glyoxal and IO from SMAX-DOAS. The AVK exhibit a well-defined peak only for the lowest layer (100 m altitude; peak value  $\sim 0.8$  for both gases). AVKs rapidly decrease for higher layers of the inversion grid. Both glyoxal and IO have about 2 DoF in the SMAX-DOAS profiles, and near-surface concentrations mark only about half of the information content from the SMAX profiles. SMAX thus can provide independent validation data for comparison with the lowest AMAX-DOAS profile data point, since the aircraft was located at about 100 m altitude above the ship during RF17. Figures 8 and 9 show the near-surface VMR for glyoxal and IO from optimal estimation. The dSCDs measured from EA + 1.5 are further converted to glyoxal and IO VMR using the parameterization approach described in Sinreich et al. (2010) and are compared in Figs. 8 and 9.



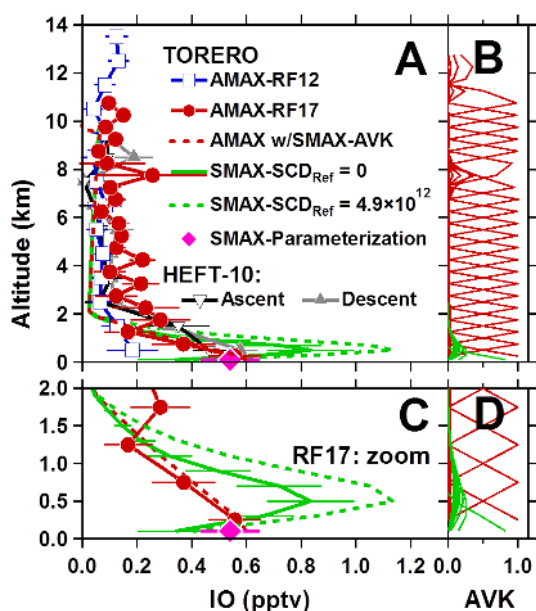


**Figure 9.** IO vertical profiles and comparison with independent validation data on the ship. (a) AMAX-DOAS during RF12 (blue squares) and RF17 (red dots) is compared with SMAX-DOAS parameterization (magenta diamond) and optimal estimation retrievals (green lines). (b) shows AVK for glyoxal from RF17 (red) and SMAX-DOAS (green). (c) is the same as (a) but with only RF17 data and zoomed for the lower 2 km. SMAX profile inversion of dSCDs is the solid green line;  $SCD_{REF} = 4.9 \times 10^{12}$  molec  $cm^{-2}$  IO is the dashed green line; simulated SMAX-DOAS view of the AMAX profile using Eq. (2) is the red dashed line; see Sect. 3.4 “Sensitivity of MAX-DOAS profiles to  $SCD_{REF}$ ” for details. (d) is the same as (b), zoomed for the lower 2 km. The error bars are based on propagating fit errors through the inversion.

The second DoF holds information about the atmospheric state aloft and is typically taken to indicate a partial VCD. Indeed, the RF17 case study provides a unique opportunity to evaluate the information content of this DoF, since the atmospheric state above the ship has been characterized by the aircraft (see above), and the radiation state is well known (Figs. 3 and 4). To our knowledge there have been no previous profile comparisons using MAX-DOAS on ships and aircraft where the true state (chemical and radiation) can be justified as well known.

### 3.4.1 Sensitivity of MAX-DOAS profiles to $SCD_{REF}$

The inverse problem to interpret ground-based MAX-DOAS data is ill posed. A confounding factor consists of the fact that the  $SCD_{REF}$  is unknown (Eq. 1). Optimal estimation trace-gas retrievals need to approximate the true atmospheric profile,  $x_t$ , with an assumption about the a priori trace-gas profile,  $x_a$  (Rogers, 2000). The products of the inversion are the retrieved profile,  $x_r$ , and the averaging kernel matrix,  $A$ ,

which describe how the  $x_r$  is related to  $x_a$  and  $x_t$ .

$$x_r = x_a + A(x_t - x_a) \quad (2)$$

MAX-DOAS profile retrievals have used atmospheric models to provide best estimates for  $x_a$ , e.g., see Franco et al. (2015). However, to our knowledge there has been no previous systematic evaluation of the effect that arises from nonzero values of  $SCD_{REF}$  (Sect. 2.8). For the RF17 case study,  $x_t$  is closely approximated by the AMAX-DOAS profiles (see Figs. 7–10), which enables us to calculate  $SCD_{REF}$  for the SMAX view. We approximate AMAX profiles as  $x_t$  for the purpose of assessing the altitude range over which SMAX data are meaningful to compare with AMAX-DOAS data. This discussion exploits knowledge of  $x_t$  in two ways: (1) we conduct a set of sensitivity studies that vary  $SCD_{REF}$  for glyoxal and IO using Eq. (1), and (2) the SMAX-view is simulated using Eq. (2) (dashed red line in Figs. 8a, c and 9a, c;  $AMAX_{SMAX-AVK}$  in Table 5). The resulting trace-gas profiles are analyzed, and the near-surface VMR and partial tropospheric VCDs are compiled in Table 5. Table 5 shows that the near-surface VMR varies by less than 10 % for glyoxal and about 20 % for IO, independent of whether the dSCDs or SCDs are used during inversion. This result is expected, given that AVK peak near 0.8 in SMAX profiles for both glyoxal and IO. The lack of sensitivity of VMR to  $SCD_{REF}$  confirms that SMAX-DOAS data provide for a meaningful comparison with AMAX-DOAS at the lowest altitudes probed by the aircraft.

However, the SMAX-VCD is very sensitive to the value of  $SCD_{REF}$ . The retrieved VCD increases systematically if nonzero values of  $SCD_{REF}$  are used to invert SMAX-DOAS data based on SCDs. The  $SCD_{REF}$  values for glyoxal and IO during RF17 are denoted in Table 5. For glyoxal the VCD in the lower 2 km almost doubles, and the agreement with  $x_t$  is within error (15 %) only when the  $SCD_{REF}$  is accounted for. Also 65 % (instead of 37 %) of the tropospheric VCD are observed from the ship. The IO VCD increased by 40 % and is systematically higher than  $x_t$  (by up to 60 % below 2 km); the agreement is surprisingly good and marginally within error for tropospheric IO VCDs (within 20 %). Figures 8c and 9c show that the SMAX simulated view of the AMAX glyoxal (and IO) profile closely resembles the SMAX measured view for glyoxal (AMAX measured view for IO). The VCD below 2 km agrees within better 4 % for glyoxal (and 15 % for IO). For comparison, the sensitivity studies show that the choice of the water cross section can affect glyoxal dSCDs by 4 % (with water residual) and IO dSCDs by 16 % (Fig. S3, Sect. 3.2.2). The SMAX data thus corroborate the robustness of glyoxal and IO dSCDs measured by AMAX.

For the purpose of AMAX-DOAS validation, we limit the use of SMAX data to the comparison of near-surface VMR. No attempts have been made to optimize the  $x_a$  or  $x_a$ -error matrices, e.g., by using AMAX profiles as  $x_a$  to avoid bias. However, it seems evident that the information content of MAX-DOAS retrievals increases towards higher alti-

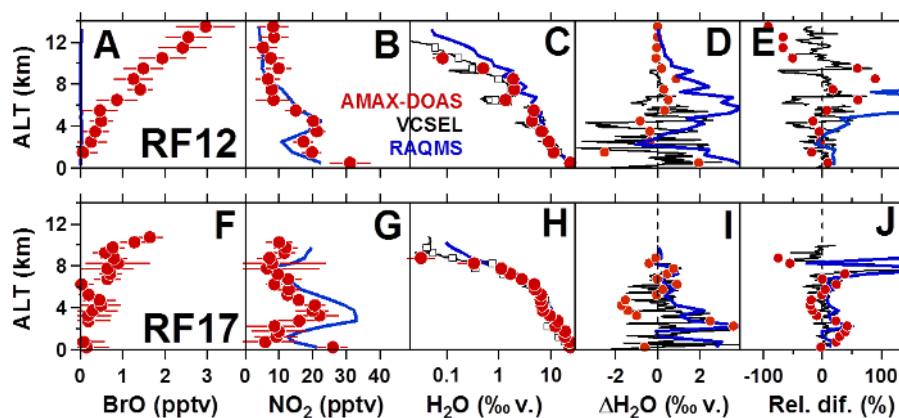


**Figure 10.** Vertical profiles of BrO, NO<sub>2</sub> and H<sub>2</sub>O and comparison with independent validation data in the form of in situ VCSEL-H<sub>2</sub>O, RAQMS-H<sub>2</sub>O and RAQMS-NO<sub>2</sub>. See Sects. 3.4, 4.2, 4.3 and 4.4 for details.

**Table 5.** Comparison of near-surface VMR and partial VCDs for CHOCHO and IO during RF17.

	SCD <sub>Ref</sub> <sup>a</sup> (molec cm <sup>-2</sup> )	VMR <sub>0.1</sub> <sup>+</sup> (pptv)	VCD <sub>MBL</sub> <sup>a</sup> (molec cm <sup>-2</sup> )	VCD <sub>trop</sub> <sup>a</sup> (molec cm <sup>-2</sup> )	ΔVMR <sub>0.1</sub> <sup>+</sup> (%)	ΔVCD <sub>MBL</sub> <sup>+</sup> (%)	ΔVCD <sub>trop</sub> <sup>+</sup> (%)
<b>CHOCHO</b>							
SMAX	0.0	32 ± 6	0.83 ± 0.19	1.00 ± 0.21	0	0	0
	3.0	34 ± 6	1.28 ± 0.19	1.47 ± 0.21	+6	+54	+47
	4.8 <sup>c</sup>	35 ± 6	1.55 ± 0.19	1.75 ± 0.21	+9	+87	+75
	6.0	36 ± 6	1.72 ± 0.19	1.94 ± 0.21	+13	+107	+94
LED-CE-DOAS <sup>b</sup>		37 ± 5					
AMAX		34 ± 8	1.63 ± 0.20	2.71 ± 0.35			
AMAX <sub>SMAX-AVK</sub>		29 ± 8	0.80 ± 0.40	0.98 ± 0.46			
<b>IO</b>							
SMAX	0.0	0.34 ± 0.14	1.81 ± 0.41	2.19 ± 0.45	0	0	0
	3.0	0.38 ± 0.14	2.28 ± 0.41	2.69 ± 0.45	+12	+26	+23
	4.9 <sup>c</sup>	0.40 ± 0.14	2.58 ± 0.41	3.00 ± 0.45	+18	+43	+37
	6.0	0.42 ± 0.14	2.75 ± 0.41	3.18 ± 0.45	+24	+52	+45
AMAX		0.55 ± 0.10	1.57 ± 0.23	2.46 ± 0.41			
AMAX <sub>SMAX-AVK</sub>		0.57 ± 0.10	1.53 ± 0.60	1.93 ± 0.53			

<sup>a</sup> SCD<sub>Ref</sub> and VCD units for IO: 10<sup>12</sup> molec cm<sup>-2</sup>; CHOCHO: 10<sup>14</sup> molec cm<sup>-2</sup>; VCD<sub>MBL</sub> is integrated from 0 to 2 km; VCD<sub>trop</sub> integral is 0–10 km (SMAX), 0–10 km (RF17), 0–13 km (RF12). Integration of AMAX 0–10 km is not different within error (10–15 % lower values).

<sup>b</sup> Volume mixing ratio near the surface. SMAX-DOAS: 0.1 km (grid box: 0 to 0.2 km); LED-CE-DOAS: 18 m altitude; AMAX-DOAS: 0.1 km = sensor altitude (grid box: 0 to 0.5 km); ΔVMR is defined as the relative increase compared to the SCD<sub>Ref</sub> = 0 molec cm<sup>-2</sup> case.

<sup>c</sup> SCD<sub>Ref</sub> calculated for the SMAX zenith reference during the AMAX overpass (see Table 1), using the AMAX trace-gas and aerosol profiles. RTM settings: EA = 90; SZA = 38.3; surface albedo = 0.1; SSA = 0.98; g = 0.74; wavelength = 428 nm (IO), 455 nm (CHOCHO).

tudes when SCD<sub>REF</sub> is known. Maximizing knowledge about SCD<sub>REF</sub> is systematically exploited for AMAX-DOAS in this study and requires independent information for ground-based MAX-DOAS. It is presently unclear whether our results, that is, 50 % of the glyoxal and IO and 95 % of tropospheric BrO VCD reside above 2 km, apply also over other terrestrial and oceanic environments.

#### 4 Discussion of AMAX-DOAS profiles

The independent validation data to assess AMAX-DOAS profiles of aerosol extinction from aerosol size distribution measurements aboard the aircraft have been discussed above (Sect. 3.1). The following sections discuss the validation of AMAX-DOAS trace-gas profiles by in situ glyoxal (fast LED-CE-DOAS), near-surface VMR of glyoxal and IO (Table 5, Sect. 4.1.1 and 4.1.3) and BrO (Sect. 4.4.1) from SMAX-DOAS; NO<sub>2</sub> predictions from RAQMS (Sect. 4.2), and in situ VCSEL-H<sub>2</sub>O on the aircraft and RAQMS-H<sub>2</sub>O

(Sect. 4.3). Given the novelty of glyoxal and BrO observations in the tropical FT, a brief discussion of literature context and atmospheric implications is further given.

## 4.1 Glyoxal and IO in the tropical marine atmosphere

### 4.1.1 Glyoxal in the MBL

The glyoxal VMR in the MBL is rather robust between three instruments. No glyoxal gradient is detectable in the lower 500 m (Fig. 8). AMAX-DOAS measured  $34 \pm 7$  pptv glyoxal at 250 m, compared to  $33 \pm 7$  and  $35 \pm 7$  pptv by SMAX-DOAS at 100 and 500 m, respectively, and  $38 \pm 5$  pptv by LED-CE-DOAS at 18 m. The in situ and remote sensing instruments use a common source of calibration, i.e., the same UV-visible absorption cross-section spectrum (Volkamer et al., 2005b). Such agreement from measurements at different spatial scales is only possible in homogeneous air, such as the remote MBL. The homogeneity is corroborated from the time resolved in situ observations (Coburn et al., 2014).

Previous studies had measured  $\sim 80$  pptv glyoxal over the Sargasso Sea by DNPH (2,4-Dinitrophenylhydrazine, Brady's reagent) derivatization/mass spectrometry detection (Zhou and Mopper, 1990), 40–80 pptv over the tEPO by SMAX-DOAS (Sinreich et al., 2010), 20–40 pptv during various cruises by SMAX-DOAS (Mahajan et al., 2014),  $32 \pm 6$  pptv (average northern hemispheric tropics) and  $47 \pm 9$  pptv (average southern hemispheric tropics) during the TORERO cruise by LED-CE-DOAS (Coburn et al., 2014), 24 pptv over the Southern Ocean and 7 pptv at Cape Grim by DNPH derivatization/high performance liquid chromatography detection (Lawson et al., 2015). Previous SMAX-DOAS measurements likely provide lower limits for the VCD because of uncertainties regarding  $\text{SCD}_{\text{REF}}$  (see Table 5). Notably, hemispheric gradients in the near-surface VMR of glyoxal in the tropics do not show a close resemblance with satellite VCDs (Coburn et al., 2014) and concentrations in the MBL by Lawson et al. (2015) do not explain the satellite VCDs near Cape Grim. Assuming the satellite measurements are correct, this could possibly suggest that our findings that most of the glyoxal VCD is located aloft could be more broadly applicable.

### 4.1.2 Glyoxal in the tropical FT

The highest glyoxal VMR is observed in the AMAX profile at 750 m altitude ( $45 \pm 7$  pptv). Our measurements further show 3–20 pptv in the tropical free troposphere. Indeed, more than 50 % of the glyoxal VCD is located above 2 km altitude. The atmospheric lifetime of glyoxal at tropical latitudes is only a few hours. A significant presence of glyoxal in air aloft is in apparent contradiction with the empirical relationship suggested by (Junge, 1974) that the variability of concentrations of volatile trace gases in air at remote loca-

tions is inversely proportional to their atmospheric residence time.

Measurements of glyoxal vertical profiles are extremely scarce, and previous measurements are limited to terrestrial environments (Lee et al., 1998; Baidar et al., 2013a). Lee et al. (1998) detected a mean of 26 pptv glyoxal in the FT (minimum: 10 pptv; maximum: 60 pptv) above areas with strong isoprene emissions over the southeastern USA. They also measured other small oxygenated VOC, like formaldehyde, methyl glyoxal and pyruvic acid. Baidar et al. (2013a) observed 5–30 pptv glyoxal between 1 and 3 km over Los Angeles, CA. Previous measurements of acetaldehyde in the FT (Singh et al., 2001; 2004; Kwan et al., 2006) are not free of controversy (Staudt et al., 2003; Singh et al., 2004; Millet et al., 2010). Small oxygenated VOC (OVOC) form from the volatilization of organic aerosol by reaction with OH radicals (Molina et al., 2004) and ozone (Thornberry and Abbatt, 2004) and provide a source for acetaldehyde and its oxidation product peroxyacetic acid in the FT (Kwan et al., 2006). Heterogeneous reaction of ozone with polyunsaturated fatty acids are a source for OVOC, including small yields of glyoxal (Zhou et al., 2014). The particular physical-chemical properties of glyoxal (high solubility and short lifetime) distinguish the tracer properties of this molecule from other OVOC (Coburn et al., 2014). Recent EC flux measurements of glyoxal during the TORERO cruise have detected positive fluxes that locate a glyoxal source inside the sea-surface microlayer (Coburn et al., 2014). However, during most of the day the EC flux was directed from the atmosphere into the ocean, thus requiring an airborne glyoxal source.

The vertical profiles of glyoxal and aerosol extinction show some resemblance that is currently under further investigation. Atmospheric models currently do not predict any appreciable concentrations of glyoxal over oceans (Fu et al., 2008; Myriokefalitakis et al., 2008), and some satellites detect glyoxal (Wittrock et al., 2006; Vrekoussis et al., 2009; Lerot et al., 2010; Alvarado et al., 2014) while others do not find significant enhancements over oceans (Chan Miller et al., 2014). The fact that glyoxal is distributed above and below cloud layers suggests that cloud slicing techniques hold some potential to investigate the glyoxal vertical distribution from space and compare with our profiles.

### 4.1.3 IO in the tropical MBL and FT

The IO VMR is generally less robust than that of glyoxal but also subject to relatively larger error bars. Generally the differences are within the combined errors of the SMAX and AMAX inversions. However, the near-surface VMR for SMAX was 40 % lower than AMAX, while the average VMR over the lower 2 km was consistently larger than AMAX by up to 60 %. This suggests that ground-based MAX-DOAS retrievals of IO are rather sensitive to retrieval settings (factor of 2–3). For AMAX-IO the better access to references that minimize  $\text{SCD}_{\text{REF}}$  seems advantageous, and

the IO vertical profiles closely approximate  $x_1$ . For example, when Eq. (2) was applied using the SMAX-AVKs to simulate the SMAX-view of the AMAX profile (Fig. 9c), the near-surface VMR and  $VCD_{\text{MBL}}$  remained unchanged (within 4 %, Table 5). Based on the comprehensive evidence we believe that AMAX-IO concentrations can be considered accurate within 20 % inside the MBL (at high signal-to-noise ratio) and likely better in dryer FT air.

The MBL-IO measured by AMAX is  $0.2 \pm 0.1$  pptv IO (RF12) and  $0.55 \pm 0.1$  pptv IO (RF17). This is generally consistent for RF17 with  $\sim 0.5$ – $0.6$  pptv IO that we had measured previously over the central Pacific (Dix et al., 2013). About 0.2 pptv IO is expected from organic iodine precursors over the open ocean (Jones et al., 2010). Previous IO observations inside the MBL showed  $\sim 1.5$  pptv at Cape Verde Islands in the tropical Atlantic Ocean (Read et al., 2008; Mahajan et al., 2010) and  $\sim 0.9$  pptv over the Eastern Pacific (Volkamer et al., 2010; Mahajan et al., 2012); such elevated IO is explained by inorganic iodine sources (Jammoul et al., 2009; Jones et al., 2010; Carpenter et al., 2013). Most of the currently available MBL-IO observations have been conducted by ground/ship-based MAX-DOAS (e.g., see overview by Saiz-Lopez et al., 2012b) with the above sensitivities (see Table 5, Fig. S3, Sect. 3.2.2). TORERO measurements of IO and  $\text{CH}_3\text{I}$  profiles over different ocean environments promise to shed more light on the need for inorganic iodine sources.

The IO VCD is  $(2.1 \pm 0.4) \times 10^{12}$  IO molec  $\text{cm}^{-2}$  during RF12 and  $(2.5 \pm 0.4) \times 10^{12}$  IO molec  $\text{cm}^{-2}$  during RF17. This is about 2 times larger than the  $\sim 1.0 \times 10^{12}$  molec  $\text{cm}^{-2}$  IO VCD that we had previously measured over the central tropical Pacific ocean (Dix et al., 2013). At 2 km we find variable IO of  $\sim 0.1$  pptv (RF12) and 0.2–0.3 pptv IO (RF17); the latter is in reasonable agreement with 0.2–0.4 pptv IO observed at Tenerife (Puentedura et al., 2012). There appears to be significant variability in the IO VCD over the Northern Hemisphere tropics and subtropics. Notably, the higher IO VCD over the tEPO is consistent in that some of the highest  $\text{CH}_3\text{I}$  concentrations observed are found over the tEPO (Yokouchi et al., 2008), where deep convection provides a transport pathway into the FT. Our results thus seem to corroborate our earlier speculations that apparent correlations between satellite IO and chlorophyll *a* could possibly be explained from the coupled effect of biological sources producing IO precursors with a longer lifetime. Among other factors, the convective redistribution of precursors and iodine recycling on aerosols are relevant to explaining IO distributions (Dix et al., 2013).

#### 4.2 Tropospheric $\text{NO}_2$ : assessing the quality of stratospheric correction

Under pristine marine conditions about 80 % of the  $\text{NO}_2$  VCD resides in the stratosphere (Fig. 5a).  $\text{NO}_2$  is a nearly ideal test gas for the purpose of assessing the stratospheric correction (Sects. 2.8, 3.2.2, Supplement). Figure 10 com-

pares AMAX- $\text{NO}_2$  with time-synchronous predictions from the RAQMS model. RF12 makes for a useful case study since (1) the comparison extended to higher altitudes than RF17, further (2) low tropospheric  $\text{NO}_2$  concentrations and (3) concentration gradients in the lower troposphere provide for a sensitive assessment of AMAX-DOAS performance and (4) the two case studies differ in that the solar zenith angle (SZA) was about 2 times higher during RF17 than RF12 (Table 2).

For both case studies, RAQMS and AMAX  $\text{NO}_2$  profiles show a close resemblance. The highest  $\text{NO}_2$  ( $\sim 25$  pptv) is observed in the MBL, and  $\text{NO}_2$  rapidly decreased above the MBL. An interim minimum is predicted by RAQMS around  $\sim 10$  pptv  $\text{NO}_2$  between 1 km (RF17) and 2.5 km (RF12). This minimum is confirmed by AMAX and well resolved only during RF17. The  $\text{NO}_2$  layer near 4 km (maximum  $\text{NO}_2 \sim 20$  pptv) is observed for both case studies, and the predicted  $\text{NO}_2$  enhancement within this layer agrees remarkably well with the observations. The minimum  $\text{NO}_2$  is predicted between 10 and 14 km, and the comparison indicates that a reliable detection of 5–10 pptv tropospheric  $\text{NO}_2$  is possible at ceiling altitude of the GV without apparent bias even at such low  $\text{NO}_2$  (agreement within error bars). In particular, no  $\text{NO}_2$  increase is observed near the ceiling altitude of the plane, confirming that MBL references provide a clean and accurate correction of stratospheric influences also at altitude. Similarly good agreement between modeled and observed  $\text{NO}_2$  profiles have been observed during the TRACE-P project (Pierce et al., 2003). The RAQMS family approach for total odd nitrogen ( $\text{NO}_y$ ), combined with NMHC chemistry appropriate for large-scale applications, accurately represents photochemically active  $\text{NO}_y$  species such as  $\text{NO}_2$  in the relatively pristine conditions sampled during TORERO.

Notably, at tropical latitudes the SZA changes more rapidly than at high latitudes. AMAX-DOAS observations are possible at SZA larger  $80^\circ$  and are rather insensitive to changes of SZA at the moderate/low SZA probed during TORERO. For example, during RF12 the SZA changed by  $4^\circ$  (mean SZA  $\sim 23.2^\circ$ ) and  $19^\circ$  (RF17: SZA decreasing from  $44.8$  to  $25.5^\circ$ ), which corresponds to a  $< 1 \times 10^{14}$  molec  $\text{cm}^{-2}$   $\text{NO}_2$  change due to changes in stratospheric photon paths. This is 10–20 times smaller than the measured dSCDs at altitude. This correction increases with SZA and can be predicted reasonably well using models. Thus changes in the SZA are not a limitation for measurements of tropospheric  $\text{NO}_2$  and BrO during TORERO. Measurements at larger SZA (e.g.,  $> 60^\circ$ ) benefit from regular access to suitable reference geometries, e.g., EA + 90 at altitudes in the lower FT (Baidar et al., 2013a).

#### 4.3 Tropospheric $\text{H}_2\text{O}$ : comparison with in situ VCSEL and RAQMS

Water vapor is a transport tracer that determines atmospheric stability. The comparison with in situ VCSEL- $\text{H}_2\text{O}$  measurements is challenging due to the different horizontal

and vertical scales that are probed (Supplement). We take the vertical resolution of AMAX into account and apply Eq. (2) (using the AVKs and  $x_a$  of IO) to smooth the in situ VCSEL-H<sub>2</sub>O profiles (Rodgers and Connor, 2003). No further averaging was applied to account for horizontal gradients in comparing VCSEL-, AMAX- and RAQMS-H<sub>2</sub>O. The smoothed VCSEL<sub>AVK</sub> profile is shown as open black squares in Fig. 10c and h. The numerical smoothing error is smaller than 7 % in all cases, as assessed from the median bias from the relative difference ( $[\text{VCSEL} - \text{VCSEL}_{\text{AVK}}] / \text{VCSEL}_{\text{AVK}}$ ) at different altitudes. For comparison the median bias for AMAX-H<sub>2</sub>O is +4.8 % (0–9 km, average of RF12: +7.4 %, and RF17: +2.2 %), with an average standard deviation of 48 % (RF12: 36 %, RF17: 59 %). Clearly, the atmospheric H<sub>2</sub>O variability is affecting the comparison, but no significant bias is observed between the calibration of VCSEL and AMAX-DOAS.

Conversely, in situ and column H<sub>2</sub>O can be used to instantaneously assess the variability in atmospheric H<sub>2</sub>O as a transport tracer in the vicinity of the aircraft. AMAX-H<sub>2</sub>O column measurements inherently average over H<sub>2</sub>O variability and provide information that is complementary to in situ H<sub>2</sub>O. The atmospheric variability is illustrated in Fig. 10d and i in the form of absolute differences between AMAX- and RAQMS-H<sub>2</sub>O to VCSEL<sub>AVK</sub>. Figure 10e and j show their relative differences. For RF12 the AMAX data scatter statistically around 0 under conditions when the relative difference in RAQMS is small. Between 6 and 10 km, relative differences are systematically positive for both AMAX and RAQMS data (note: RAQMS-H<sub>2</sub>O is off-scale in Fig. 10e and j). The aircraft was surrounded by air that was on average 55 % dryer than the regional average H<sub>2</sub>O. Interestingly, the BrO profile begins to steepen in these relatively dryer air masses.

## 4.4 Tropospheric BrO

### 4.4.1 BrO in the MBL

Our data provide a unique perspective about BrO in the MBL over remote oceans. We found no evidence for significant MBL-BrO on the ship and aircraft when comparing limb and zenith spectra recorded inside the MBL (see also Sect. 3.2.1). This indicates that there is no BrO above our detection limit in the MBL. For comparison, results from radiative transfer calculations where we added 0.5 and 1.0 pptv BrO, respectively, into the lower kilometer/MBL show a significant positive offset (see red dashed/dotted lines in Fig. 5c). The comparison of different references in the aircraft data holds additional information to infer information about BrO in the MBL. The limb spectra are maximally sensitive towards BrO in the MBL, while the EA – 10 spectra at altitude are virtually insensitive towards BrO in the MBL (Fig. 5a). If there was significant BrO in the MBL, the intrinsic offset derived from the measurements should be

smaller than that calculated from the RTM. However, we find the agreement is excellent. The offsets in comparing limb and EA – 10 during RF12 ( $-7.2 \pm 0.5 \times 10^{13}$  molec cm<sup>-2</sup>) is consistent with that expected from the RTM of our RF12-BrO profile (RF12:  $-5.6 \pm 1.2 \times 10^{13}$  molec cm<sup>-2</sup>, Fig. 5c). Within error the difference of the experimental and calculated offset is compatible with 0 BrO and no more than  $0.5\text{--}1.6 \times 10^{13}$  molec cm<sup>-2</sup> BrO dSCD. This is comparable or smaller than the scatter we find between choosing different MBL zenith references. Given the comprehensive evidence we conclude that BrO in the MBL was generally below our detection limit ( $\sim 0.5$  pptv) and certainly below 1 pptv in all cases. Based on the insignificant BrO in the MBL and the consistency between the measured and calculated offsets we chose MBL limb spectra as our references, as they provide the most stable analysis. If there was BrO in the MBL, our inferred concentrations would be lower limits.

### 4.4.2 Tropospheric BrO vertical profiles in the tropics

The tropospheric BrO VCD from our profiles corresponds to  $1.5 \pm 0.4 \times 10^{13}$  molec cm<sup>-2</sup> for RF12 and a lower limit of  $0.5 \times 10^{13}$  molec cm<sup>-2</sup> during RF17. At 10.5 km altitude the VMR was 1.6 pptv BrO during RF17, which is only slightly lower than the 2.3 pptv BrO measured at comparable altitude during RF12. Atmospheric models currently predict lower BrO (0.2–0.5 pptv) in the tropical FT, and tropospheric BrO VCDs of  $0.2\text{--}1.0 \times 10^{13}$  molec cm<sup>-2</sup> (Parrélla et al., 2012; Saiz-Lopez et al., 2012a) are in reasonable agreement with upper limit tropospheric BrO VCDs of  $0.2\text{--}0.3 \times 10^{13}$  molec cm<sup>-2</sup> from direct-sun balloon measurements (Pundt et al., 2002; Dorf et al., 2008). However, these measurements are 3–10 times lower than column observations of tropospheric BrO from ground and satellites (Chance, 1998; Fitzenberger et al., 2000; Wagner et al., 2001; Richter et al., 2002; Van Roozendael et al., 2002; Salawitch et al., 2005; Hendrick et al., 2007; Theys et al., 2007, 2011; Coburn et al., 2011), including measurements in the tropics (Salawitch et al., 2005; Theys et al., 2007, 2011; Coburn et al., 2011) that consistently point to the existence of a – possibly ubiquitous – tropospheric BrO background concentration of  $1\text{--}3 \times 10^{13}$  molec cm<sup>-2</sup> BrO VCD. There is no previous corroborating evidence from a measurement in the tropical FT to resolve this conundrum between existing measurements (Supplement). The BrO VCD from RF12 is 12 % lower than the equivalent VCD to 1 pptv BrO throughout the troposphere (Salawitch et al., 2005) (corresponds to  $1.7 \times 10^{13}$  molec cm<sup>-2</sup> below 13 km) and closely resembles the January/February average BrO VCD measured by the GOME-2 satellite ( $\sim 1.6 \times 10^{13}$  molec cm<sup>-2</sup>, 30° N–30° S) (Theys et al., 2011) and  $\sim 2 \times 10^{13}$  molec cm<sup>-2</sup> BrO VCD at Pensacola, FL (Coburn et al., 2011). Our tropospheric BrO column amounts are consistent with satellite and ground-based observations at tropical latitudes (Salawitch et al., 2005; Theys et al., 2007, 2011; Coburn et al., 2011) and

add consistent BrO profile information to the comprehensive evidence that supports the presence of a global background concentration of tropospheric BrO in considerable amounts (WMO, 2010). Our results suggest that the impact of halogens on tropospheric ozone and the oxidation of atmospheric mercury is currently underestimated.

## 5 Conclusions

Limb observations of solar scattered photons by CU AMAX-DOAS provide sensitive and robust measurements of tropospheric BrO, IO and glyoxal profiles at tropical latitudes during aircraft ascents/descents, as well as of NO<sub>2</sub>, H<sub>2</sub>O and O<sub>4</sub> (multispectral aerosol extinction). In principle, other gases can also be measured, like formaldehyde (HCHO) or nitrous acid (HONO). CU AMAX-DOAS observations are optimized to (1) locate BrO, IO and glyoxal in the troposphere, (2) decouple stratospheric absorbers, (3) maximize sensitivity at instrument altitude, (4) facilitate altitude control and (5) enable observations over a wide range of SZA.

We present the first evaluation of the AMAX-DOAS technique by means of vertically resolving HSRL and in situ measurements from UHSAS aerosol size-distributions and VCSEL H<sub>2</sub>O. Information about aerosol extinction profiles is prerequisite to the trace-gas retrieval. We conclude the following.

- The accuracy of O<sub>4</sub> dSCD measurements is not significantly impacted by the presence of aerosols. This extends our previous assessments of O<sub>4</sub> in a Rayleigh atmosphere (Spinei et al., 2015) towards an aerosol laden atmosphere and demonstrates that O<sub>4</sub> correction factors (Wagner et al., 2009; and references in Spinei et al., 2015) are not needed to interpret CU AMAX-DOAS data (error < 6 %). The accuracy of O<sub>4</sub> SCDs in the presence of aerosols under controlled conditions (Thalman and Volkamer, 2010) is thus confirmed from field data. O<sub>4</sub> dSCDs constraints to infer aerosol extinction profiles are straightforward.
  - The aerosol extinction profile from the O<sub>4</sub> band at 477 nm has excellent signal-to-noise ratio. We find reasonable agreement with HSRL<sub>477</sub>. The comparison with Mie calculations of in situ aerosol size distributions shows good agreement only in terms of the relative profile shape. A quantitative radiation closure required scaling of the Mie calculations (by a factor of ~ 10–13). The reason for this factor is currently not understood and deserves further investigation.
  - The AMAX-H<sub>2</sub>O profiles show no evidence for bias after the difference in vertical resolution has been accounted for by applying the AMAX-AVKs to the in situ H<sub>2</sub>O data (error ~ 7 %). This demonstrates good control over RTM.
  - Water is a transport tracer. Column and in situ H<sub>2</sub>O provide complementary information to characterize H<sub>2</sub>O variability/H<sub>2</sub>O gradients in the air surrounding the aircraft. AMAX-H<sub>2</sub>O column averages sample over spatial scales that compare more closely to the scales observed by satellites and predicted by atmospheric models (Fig. 10, Sect. 4.3, Supplement).
- For BrO, IO and glyoxal profiles we evaluate the robustness of dSCDs as a function of altitude and compare with ship-based in situ LED-CE-DOAS (glyoxal) and ship MAX-DOAS inside the MBL. We conclude the following.
- Our limb measurements have about 500 m vertical resolution (RF17) and 12–13 DoF for tropospheric BrO, 14–20 DoF for IO, 12–17 DoF for glyoxal and 13–20 DoF for NO<sub>2</sub>. For comparison, the SMAX-DOAS retrieval has about 2.0 DoF for glyoxal and IO. The ship measurements provide independent validation data only near the surface.
  - For IO and glyoxal, EA0 (limb) or EA + 10 spectra near ceiling altitude have SCD<sub>REF</sub> values that are smaller than the dSCD measurement error of spectra at lower altitudes. For BrO and NO<sub>2</sub> the SCD<sub>REF</sub> is minimized for MBL EA0 (BrO) or MBL EA + 90 (zenith, NO<sub>2</sub>) references. The accurate correction of stratospheric NO<sub>2</sub> and BrO is demonstrated by the good agreement of 5–10 pptv NO<sub>2</sub> at 14.5 km with RAQMS NO<sub>2</sub> (see Sect. 4.2), confirming that dSCDs can be treated de facto as tropospheric SCDs.
  - Reference spectra recorded at different altitudes/geometries result in dSCD offsets that are understood within error from our a posteriori BrO, IO and glyoxal profiles. This corroborates the robustness of measured dSCDs, i.e., rules out systematic factors that depend on altitude to affect our profiles (e.g., Raman scattering).
  - No BrO was detected inside the MBL by either ship or AMAX-DOAS. For glyoxal, in situ and two remote-sensing techniques agree within 10 % in the lower 250 m; two further remote measurements agree within 30 % for IO. We find no significant evidence for gradients in glyoxal in the lower 2 km, while IO decreases rapidly above 500m during RF17.
  - For ship MAX-DOAS there is considerable sensitivity in the VCDs and profile shapes depending on whether dSCDs or SCDs are used during inversion. The value of SCD<sub>REF</sub> is initially unknown. RF17 is to our knowledge the first profile comparison for which independent information about SCD<sub>REF</sub> is available. SMAX underestimated glyoxal VCDs (factor 2–3) and overestimated IO VCDs (up to 60 %); the best agreement was found with



SCD<sub>REF</sub> constrained based on the aircraft data. Maximizing knowledge about SCD<sub>REF</sub> holds largely unexplored potential to access information about the FT from ground-based MAX-DOAS.

Much of the current knowledge of bromine chemistry in the upper troposphere–lower stratosphere (UTLS) is based on balloon-borne direct-sun BrO measurements (Pundt et al., 2002; Dorf et al., 2008; Supplement). If the elevated BrO found in this study applies more broadly a reassessment of halogen chemistry in the UTLS is needed. Furthermore, the presence of glyoxal in the tropical FT is a smoking gun for other OVOC species and has the potential to modify tropospheric HO<sub>x</sub> and NO<sub>x</sub>, O<sub>3</sub> and aerosols. Our understanding of the chemical processes involving halogens and organic carbon species in the tropics seems incomplete.

## Appendix A: List of frequently used abbreviations.

---

AMAX-DOAS	airborne MAX-DOAS
AMF	air mass factor
AOD	aerosol optical depth
AVK	averaging kernel
Box-AMF	box air mass factors
BrO	bromine monoxide
CE-DOAS	cavity-enhanced DOAS
CHOCHO	glyoxal
CO	carbon monoxide
CU	University of Colorado
dAMF	differential air mass factor
DOAS	differential optical absorption spectroscopy
DoF	degrees of freedom
dSCD	differential slant column density
EA	elevation angle
FWHM	full width at half maximum
FT	free troposphere
GDAS	global data assimilation system
GV	Gulfstream V aircraft
HCHO	formaldehyde
IO	iodine monoxide
KA	Ka'imimoana research vessel
LED-CE-DOAS	light-emitting-diode cavity-enhanced DOAS
LTM	Langley trajectory model
MAX-DOAS	Multi-AXis DOAS
MBL	marine boundary layer
MFC DOAS	software package
McArtim	Monte Carlo radiative transfer model
NCEP	National Centers for Environmental Prediction
NO <sub>2</sub>	nitrogen dioxide
O <sub>4</sub>	oxygen collision pair, O <sub>2</sub> -O <sub>2</sub>
OVOC	oxygenated volatile organic compound
PBL	planetary boundary layer
ppbv	parts per billion by volume; 1 ppbv = 2.2 × 10 <sup>10</sup>
RAQMS	Real-time Air Quality Modeling System
RDF	reverse domain filling
RF12	research flight 12
RF17	research flight 17
RTM	radiative transfer model
RMS	root mean square
SCD	slant column density
SCD <sub>REF</sub>	SCD in the reference spectrum
SMAX-DOAS	ship MAX-DOAS
SOA	secondary organic aerosol
SOLAS	Surface Ocean Lower Atmosphere Study
SSA	single scattering albedo
SZA	solar zenith angle
TORERO	Tropical Ocean tRoposphere Exchange of Reactive halogens and Oxygenated hydrocarbons
UHSAS	ultra high sensitivity aerosol spectrometer
UT	upper troposphere
UTLS	upper troposphere-lower stratosphere
VCD	vertical column density
VCSEL	vertical-cavity surface-emitting laser hygrometer
VMR	volume mixing ratio
VOC	volatile organic compound
Z	altitude

---

The Supplement related to this article is available online at doi:10.5194/amt-8-2121-2015-supplement.

**Acknowledgements.** The TORERO project is funded by the National Science Foundation under award AGS-1104104 (PI: R. Volkamer). The involvement of the NSF-sponsored Lower Atmospheric Observing Facilities, managed and operated by the National Center for Atmospheric Research (NCAR) Earth Observing Laboratory (EOL), is acknowledged. We thank Jorgen Jensen and Mathew Hayman for helpful discussions. S. Wang is a recipient of the Fulbright Junior Research Award; S. Baidar is a recipient of ESRL/CIRES graduate fellowship. R. Volkamer acknowledges financial support from National Science Foundation Faculty Early Career Development (CAREER) award ATM-0847793, Department of Energy award DE-SC0006080 and Electric Power Research Institute (EPRI) contracts EP-P27450/C13049 and EP-P32238/C14974 that supported the development of the AMAX-DOAS instrument and software/data analysis tools used in this study.

**Disclaimer.** The views, opinions and findings contained in this report are those of the author(s) and should not be construed as an official National Oceanic and Atmospheric Administration or US government position, policy or decision.

Edited by: L. Carpenter

## References

- Aliwell, S. R., Van Roozendaal, M., Johnston, P. V., Richter, A., Wagner, T., Arlander, D. W., Burrows, J. P., Fish, D. J., Jones, R. L., Tørnkqvist, K. K., Lambert, J.-C., Pfeilsticker, K., and Pundt, I.: Analysis for BrO in zenith-sky spectra: An intercomparison exercise for analysis improvement, *J. Geophys. Res.-Atmos.*, 107, ACH 10-1–ACH 10-20 doi:10.1029/2001JD000329, 2002.
- Alvarado, L. M. A., Richter, A., Vrekoussis, M., Wittrock, F., Hilboll, A., Schreier, S. F., and Burrows, J. P.: An improved glyoxal retrieval from OMI measurements, *Atmos. Meas. Tech.*, 7, 4133–4150, doi:10.5194/amt-7-4133-2014, 2014.
- Apel, E., Hills, A., Lueb, R., Zindel, S., Eisele, S., and Riemer, D.: A fast-GC/MS system to measure C2 to C4 carbonyls and methanol aboard aircraft, *J. Geophys. Res.-Atmos.*, 108, 8794, doi:10.1029/2002JD003199, 2003.
- Apel, E. C., Emmons, L. K., Karl, T., Flocke, F., Hills, A. J., Madronich, S., Lee-Taylor, J., Fried, A., Weibring, P., Walega, J., Richter, D., Tie, X., Mauldin, L., Campos, T., Weinheimer, A., Knapp, D., Sive, B., Kleinman, L., Springston, S., Zaveri, R., Ortega, J., Voss, P., Blake, D., Baker, A., Warneke, C., Welsh-Bon, D., de Gouw, J., Zheng, J., Zhang, R., Rudolph, J., Junkermann, W., and Riemer, D. D.: Chemical evolution of volatile organic compounds in the outflow of the Mexico City Metropolitan area, *Atmos. Chem. Phys.*, 10, 2353–2375, doi:10.5194/acp-10-2353-2010, 2010.
- Baidar, S., Oetjen, H., Coburn, S., Dix, B., Ortega, I., Sinreich, R., and Volkamer, R.: The CU Airborne MAX-DOAS instrument: vertical profiling of aerosol extinction and trace gases, *Atmos. Meas. Tech.*, 6, 719–739, doi:10.5194/amt-6-719-2013, 2013a.
- Baidar, S., Volkamer, R., Alvarez, R., Brewer, A., Davies, F., Langford, A., Oetjen, H., Pearson, G., Senff, C., and Hardesty, R.M.: Combining Active and Passive Airborne Remote Sensing to Quantify NO<sub>2</sub> and O<sub>x</sub> Production near Bakersfield, CA, *British Journal for Environmental and Climate Change*, 3, 2013, 566–586, doi:10.9734/BJECC/2013/5740, 2013b.
- Bogumil, K., Orphal, J., Homann, T., Voigt, S., Spietz, P., Fleischmann, O., Vogel, A., Hartmann, M., Kromminga, H., Bovensmann, H., and Burrows, J.P.: Measurements of molecular absorption spectra with the SCIAMACHY pre-flight model: Instrument characterization and reference data for atmospheric remote-sensing in the 230–2380 nm region, *J. Photoch. Photobio. A*, 157, 167–184, 2003.
- Bruns, M., Buehler, S. A., Burrows, J. P., Richter, A., Rozanov, A., Wang, P., Heue, K. P., Platt, U., Pundt, I., and Wagner, T.: NO<sub>2</sub> Profile retrieval using airborne multi axis UV-visible skylight absorption measurements over central Europe, *Atmos. Chem. Phys.*, 6, 3049–3058, doi:10.5194/acp-6-3049-2006, 2006.
- Cai, Y., Montague, D., Mooiweer-Bryan, W., and Deshler, T.: Performance characteristics of the ultra high sensitivity aerosol spectrometer for particles between 55 and 800 nm: Laboratory and field studies, *J. Aerosol Sci.*, 39, 759–769, 2008.
- Carlton, A. G., Turpin, B. J., Altieri, K. E., Seitzinger, S., Reff, A., Lim, H. J., and Ervens, B.: Atmospheric oxalic acid and SOA production from glyoxal: Results of aqueous photooxidation experiments, *Atmos. Environ.*, 41, 7588–7602, 2007.
- Carpenter, L. J., MacDonald, S. M., Shaw, M. D., Kumar, R., Saunders, R. W., Parthipan, R., Wilson, J., and Plane, J. M.: Atmospheric iodine levels influenced by sea surface emissions of inorganic iodine, *Nature Geosci.*, 6, 108–111, doi:10.1038/ngeo1687, 2013.
- Chan Miller, C., Gonzalez Abad, G., Wang, H., Liu, X., Kurosu, T., Jacob, D. J., and Chance, K.: Glyoxal retrieval from the Ozone Monitoring Instrument, *Atmos. Meas. Tech.*, 7, 3891–3907, doi:10.5194/amt-7-3891-2014, 2014.
- Chance, K.: Analysis of BrO measurements from the Global Ozone Monitoring Experiment, *Geophys. Res. Lett.*, 25, 3335–3338, 1998.
- Chin, M., Ginoux, P., Kinne, S., Torres, O., Holben, B. N., Duncan, B. N., Martin, R. V., Logan, J. A., Higurashi, A., and Nakajima, T.: Tropospheric aerosol optical thickness from the GO-CART model and comparisons with satellite and sunphotometer measurements, *J. Atmos. Sci.*, 59, 461–483, doi:10.1175/1520-0469(2002)059<0461:TAOTFT>2.0.CO;2, 2002.
- Chin, M., Ginoux, P., Lucchesi, R., Huebert, B., Weber, R., Anderson, T., Masonis, S., Blomquist, B., Bandy, A., Thornton, D.: A global aerosol model forecast for the ACE-Asia field experiment, *J. Geophys. Res.*, 108, 8654, doi:10.1029/2003JD003642, 2003.
- Clémer, K., Van Roozendaal, M., Fayt, C., Hendrick, F., Hermans, C., Pinardi, G., Spurr, R., Wang, P., and De Mazière, M.: Multiple wavelength retrieval of tropospheric aerosol optical properties from MAXDOAS measurements in Beijing, *Atmos. Meas. Tech.*, 3, 863–878, doi:10.5194/amt-3-863-2010, 2010.
- Coburn, S., Dix, B., Sinreich, R., and Volkamer, R.: The CU ground MAX-DOAS instrument: characterization of RMS noise limitations and first measurements near Pensacola, FL of

- BrO, IO, and CHOCHO, *Atmos. Meas. Tech.*, 4, 2421–2439, doi:10.5194/amt-4-2421-2011, 2011.
- Coburn, S., Ortega, I., Thalman, R., Blomquist, B., Fairall, C. W., and Volkamer, R.: Measurements of diurnal variations and eddy covariance (EC) fluxes of glyoxal in the tropical marine boundary layer: description of the Fast LED-CE-DOAS instrument, *Atmos. Meas. Tech.*, 7, 3579–3595, doi:10.5194/amt-7-3579-2014, 2014.
- Collins, D.R., Jonsson, H.H., Seinfeld, J. H., Flagan, R. C., Gasso, S., Hegg, D. A., Russell, P. B., Schmid, B., Livingston, J. M., Ostrom, E.O., Noone, K. J., Russell, L. M., and Putaud, J. P.: In situ aerosol-size distributions and clear-column radiative closure during ACE-2, *Tellus B*, 52, 498–525, 2000.
- Denning, R. F., Guidero, S. L., Parks, G. S., and Gary, B. L.: Instrument description of the airborne microwave temperature profiler, *J. Geophys. Res.-Atmos.*, 94, 16757–16765, 1989.
- Deutschmann, T., Beirle, S., Frieß, U., Grzegorski, M., Kern, C., Kritten, L., Platt, U., Prados-Román, C., Wagner, T., and Werner, B.: The Monte Carlo atmospheric radiative transfer model McArtim: Introduction and validation of Jacobians and 3D features, *J. Quant. Spectrosc. Ra.*, 112, 1119–1137, 2011.
- Dix, B., Brenninkmeijer, C. A. M., Frieß, U., Wagner, T., and Platt, U.: Airborne multi-axis DOAS measurements of atmospheric trace gases on CARIBIC long-distance flights, *Atmos. Meas. Tech.*, 2, 639–652, doi:10.5194/amt-2-639-2009, 2009.
- Dix, B., Baidar, S., Bresch, J. F., Hall, S. R., Schmidt, K. S., Wang, S., and Volkamer, R.: Detection of iodine monoxide in the tropical free troposphere, *Proc. Natl. Acad. Sci. USA*, 110, 2035–2040, doi:10.1073/pnas.1212386110, 2013.
- Dorf, M., Butz, A., Camy-Peyret, C., Chipperfield, M. P., Kritten, L., and Pfeilsticker, K.: Bromine in the tropical troposphere and stratosphere as derived from balloon-borne BrO observations, *Atmos. Chem. Phys.*, 8, 7265–7271, doi:10.5194/acp-8-7265-2008, 2008.
- Eckman, R. S., Grose, W. L., Turner, R. E., Blackshear, W. T., Russell III, J. M., Froidevaux, L., Waters, J. W., Kumer, J. B., and Roche, A. E.: Stratospheric trace constituents simulated by a three-dimensional general circulation model: Comparison with UARS data, *J. Geophys. Res.*, 100, 13951–13966, 1995.
- Eloranta, E. W.: High Spectral Resolution Lidar, in: *Lidar: Range-Resolved Optical Remote Sensing of the Atmosphere*, edited by: Weitkamp, K., Springer Series in Optical Sciences, Springer-Verlag, New York, 143–163, 2005.
- Fayt, C. and Van Roozendael, M.: WinDOAS 2.1–Software user manual, Belgium, BIRA-IASB, 2001.
- Fitzenberger, R., Bosch, H., Camy-Peyret, C., Chipperfield, M. P., Harder, H., Platt, U., Sinnhuber, B. M., Wagner, T., and Pfeilsticker, K.: First profile measurements of tropospheric BrO, *Geophys. Res. Lett.*, 27, 2921–2924, 2000.
- Franco, B., Hendrick, F., Van Roozendael, M., Müller, J.-F., Stavrakou, T., Marais, E. A., Bovy, B., Bader, W., Fayt, C., Hermans, C., Lejeune, B., Pinardi, G., Servais, C., and Mahieu, E.: Retrievals of formaldehyde from ground-based FTIR and MAX-DOAS observations at the Jungfraujoch station and comparisons with GEOS-Chem and IMAGES model simulations, *Atmos. Meas. Tech.*, 8, 1733–1756, doi:10.5194/amt-8-1733-2015, 2015.
- Friess, U., Monks, P. S., Remedios, J. J., Rozanov, A., Sinreich, R., Wagner, T., and Platt, U.: MAX-DOAS O<sub>4</sub> measurements: A new technique to derive information on atmospheric aerosols: 2. Modeling studies, *J. Geophys. Res.-Atmos.*, 111, D14203, doi:10.1029/2005JD006618, 2006.
- Fu, T. M., Jacob, D. J., Wittrock, F., Burrows, J. P., Vrekoussis, M., and Henze, D. K.: Global budgets of atmospheric glyoxal and methylglyoxal, and implications for formation of secondary organic aerosols, *J. Geophys. Res.-Atmos.*, 113, D15303, doi:10.1029/2007JD009505, 2008.
- Gomer, T., Brauers, T., Heintz, F., Stutz, J., and Platt, U.: MFC User Manual, Vers. 1.98, Institut für Umwelphysik, Universität Heidelberg, 1–173, 1993.
- Hendrick, F., Van Roozendael, M., Chipperfield, M. P., Dorf, M., Goutail, F., Yang, X., Fayt, C., Hermans, C., Pfeilsticker, K., Pommerehne, J.-P., Pyle, J. A., Theys, N., and De Mazière, M.: Retrieval of stratospheric and tropospheric BrO profiles and columns using ground-based zenith-sky DOAS observations at Harestua, 60° N, *Atmos. Chem. Phys.*, 7, 4869–4885, doi:10.5194/acp-7-4869-2007, 2007.
- Heue, K.-P., Richter, A., Bruns, M., Burrows, J. P., v. Friedeburg, C., Platt, U., Pundt, I., Wang, P., and Wagner, T.: Validation of SCIAMACHY tropospheric NO<sub>2</sub>-columns with AMAXDOAS measurements, *Atmos. Chem. Phys.*, 5, 1039–1051, doi:10.5194/acp-5-1039-2005, 2005.
- Heue, K.-P., Brenninkmeijer, C. A. M., Baker, A. K., Rauthe-Schöch, A., Walter, D., Wagner, T., Hörmann, C., Sihler, H., Dix, B., Frieß, U., Platt, U., Martinsson, B. G., van Velthoven, P. F. J., Zahn, A., and Ebinghaus, R.: SO<sub>2</sub> and BrO observation in the plume of the Eyjafjallajökull volcano 2010: CARIBIC and GOME-2 retrievals, *Atmos. Chem. Phys.*, 11, 2973–2989, doi:10.5194/acp-11-2973-2011, 2011.
- Heue, K.-P., Riede, H., Walter, D., Brenninkmeijer, C. A. M., Wagner, T., Frieß, U., Platt, U., Zahn, A., Stratmann, G., and Ziereis, H.: CARIBIC DOAS observations of nitrous acid and formaldehyde in a large convective cloud, *Atmos. Chem. Phys.*, 14, 6621–6642, doi:10.5194/acp-14-6621-2014, 2014.
- Irie, H., Takashima, H., Kanaya, Y., Boersma, K. F., Gast, L., Wittrock, F., Brunner, D., Zhou, Y., and Van Roozendael, M.: Eight-component retrievals from ground-based MAX-DOAS observations, *Atmos. Meas. Tech.*, 4, 1027–1044, doi:10.5194/amt-4-1027-2011, 2011.
- Jammoul, A., Dumas, S., D’Anna, B., and George, C.: Photoinduced oxidation of sea salt halides by aromatic ketones: a source of halogenated radicals, *Atmos. Chem. Phys.*, 9, 4229–4237, doi:10.5194/acp-9-4229-2009, 2009.
- Jones, C. E., Hornsby, K. E., Sommariva, R., Dunk, R. M., von Glasow, R., McFiggans, G., and Carpenter, L. J.: Quantifying the contribution of marine organic gases to atmospheric iodine, *Geophys. Res. Lett.*, 37, L18804, doi:10.1029/2010GL043990, 2010.
- Junge, C. E.: Residence Time and Variability of Tropospheric Trace Gases, *Tellus*, 26, 477–488, 1974.
- Kampf, C. J., Waxman, E. M., Slowik, J. G., Dommen, J., Pfaffenberger, L., Praplan, A. P., Prévôt, A. S. H., Baltensperger, U., Hoffmann, T., and Volkamer, R.: Effective Henry’s Law Partitioning and the Salting Constant of Glyoxal in Aerosols Containing Sulfate, *Environ. Sci. Technol.*, 47, 4236–4244, 2013.
- Knote, C., Hodzic, A., Jimenez, J. L., Volkamer, R., Orlando, J. J., Baidar, S., Brioude, J., Fast, J., Gentner, D. R., Goldstein, A. H., Hayes, P. L., Knighton, W. B., Oetjen, H., Setyan, A., Stark, H., Thalman, R., Tyndall, G., Washenfelder, R., Waxman, E., and

- Zhang, Q.: Simulation of semi-explicit mechanisms of SOA formation from glyoxal in aerosol in a 3-D model, *Atmos. Chem. Phys.*, 14, 6213–6239, doi:10.5194/acp-14-6213-2014, 2014.
- Kraus, S.: DOASIS - A Framework design for DOAS, PhD Thesis, University of Heidelberg, Heidelberg, Germany, available at: [http://hci.iwr.uni-heidelberg.de/publications/dip/2006/Kraus\\_PhD2006.pdf](http://hci.iwr.uni-heidelberg.de/publications/dip/2006/Kraus_PhD2006.pdf), 2006.
- Kurtén, T., Elm, J., Prisle, N., Mikkelsen, K., Kampf, C., Waxman, E., and Volkamer, R.: A computational study of the effect of glyoxal – sulfate clustering on the Henry's law coefficient of glyoxal, *J. Phys. Chem. A*, doi:10.1021/jp510304c, in press, 2014.
- Kwan, A. J., Crouse, J. D., Clarke, A. D., Shinzuka, Y., Anderson, B. E., Crawford, J. H., Avery, M. A., McNaughton, C. S., Brune, W. H., Singh, H. B., and Wennberg, P. O.: On the flux of oxygenated volatile organic compounds from organic aerosol oxidation, *Geophys. Res. Lett.*, 33, L15815, doi:10.1029/2006GL026144, 2006.
- Langford, A. O., Schofield, R., Daniel, J. S., Portmann, R. W., Melamed, M. L., Miller, H. L., Dutton, E. G., and Solomon, S.: On the variability of the Ring effect in the near ultraviolet: understanding the role of aerosols and multiple scattering, *Atmos. Chem. Phys.*, 7, 575–586, doi:10.5194/acp-7-575-2007, 2007.
- Lawson, S. J., Selleck, P. W., Galbally, I. E., Keywood, M. D., Harvey, M. J., Lerot, C., Helmig, D., and Ristovski, Z.: Seasonal in situ observations of glyoxal and methylglyoxal over the temperate oceans of the Southern Hemisphere, *Atmos. Chem. Phys.*, 15, 223–240, doi:10.5194/acp-15-223-2015, 2015.
- Lee, Y. N., Zhou, X., Kleinman, L. I., Nunnermacker, L. J., Springston, S. R., Daum, P. H., Newman, L., Keigley, W. G., Holdren, M. W., Spicer, C. W., Young, V., Fu, B., Parrish, D. D., Holloway, J., Williams, J., Roberts, J. M., Ryerson, T. B., and Fehsenfeld, F. C.: Atmospheric chemistry and distribution of formaldehyde and several multioxygenated carbonyl compounds during the 1995 Nashville Middle Tennessee Ozone Study, *J. Geophys. Res.-Atmos.*, 103, 22449–22462, 1998.
- Lelieveld, J., Crutzen, P. J., and Dentener, F. J.: Changing concentration, lifetime and climate forcing of atmospheric methane, *Tellus B*, 50, 128–150, 1998.
- Lerot, C., Stavrakou, T., De Smedt, I., Müller, J.-F., and Van Roozendaal, M.: Glyoxal vertical columns from GOME-2 backscattered light measurements and comparisons with a global model, *Atmos. Chem. Phys.*, 10, 12059–12072, doi:10.5194/acp-10-12059-2010, 2010.
- Lim, B., Mahoney, M. J., Haggerty, J., and Denning, R.: The microwave temperature profiler performance in recent airborne campaigns, in: Proceedings of the IEEE International Geoscience and Remote Sensing Symposium, Melbourne, Australia, 21–26 July 2013, TH2.111.1, 2013.
- Mahajan, A. S., Plane, J. M. C., Oetjen, H., Mendes, L., Saunders, R. W., Saiz-Lopez, A., Jones, C. E., Carpenter, L. J., and McFiggans, G. B.: Measurement and modelling of tropospheric reactive halogen species over the tropical Atlantic Ocean, *Atmos. Chem. Phys.*, 10, 4611–4624, doi:10.5194/acp-10-4611-2010, 2010.
- Mahajan, A. S., Gómez Martín, J. C., Hay, T. D., Royer, S.-J., Yvon-Lewis, S., Liu, Y., Hu, L., Prados-Roman, C., Ordóñez, C., Plane, J. M. C., and Saiz-Lopez, A.: Latitudinal distribution of reactive iodine in the Eastern Pacific and its link to open ocean sources, *Atmos. Chem. Phys.*, 12, 11609–11617, doi:10.5194/acp-12-11609-2012, 2012.
- Mahajan, A. S., Prados-Roman, C., Hay, T. D., Lampel, J., Pöhler, D., Grossmann, K., Tschirner, J., Friess, U., Platt, U., Johnston, P., Kreher, K., Wittrock, F., Burrows, J. P., Plane, J. M. C., and Saiz-Lopez, A.: Glyoxal observations in the global marine boundary layer, *J. Geophys. Res.-Atmos.*, 119, 6160–6169, doi:10.1002/2013JD021388, 2014.
- Massie, S. T. and Hervig, M.: HITRAN 2012 refractive indices, *J. Quant. Spectrosc. Ra.*, 130, 373–380, 2013.
- Melamed, M. L., Solomon, S., Daniel, J. S., Langford, A. O., Portmann, R. W., Ryerson, T. B., Nicks, D. K., and Mckeen, S. A.: Measuring reactive nitrogen emissions from point sources using visible spectroscopy from aircraft, *J. Environ. Monitor.*, 5, 29–34, 2003.
- Melamed, M. L., Langford, A. O., Daniel, J. S., Portmann, R. W., Miller, H. L., Eubank, C. S., Schofield, R., Holloway, J., and Solomon, S.: Sulfur dioxide emission flux measurements from point sources using airborne near ultraviolet spectroscopy during the New England Air Quality Study 2004, *J. Geophys. Res.-Atmos.*, 113, D02305, doi:10.1029/2007JD008923, 2008.
- Meller, R. and Moortgat, G. K.: Temperature dependence of the absorption cross sections of formaldehyde between 223 and 323 K in the wavelength range 225–375 nm, *J. Geophys. Res.-Atmos.*, 105, 7089–7101, 2000.
- Merlaud, A., Van Roozendaal, M., Theys, N., Fayt, C., Hermans, C., Quennehen, B., Schwarzenboeck, A., Ancellet, G., Pommier, M., Pelon, J., Burkhardt, J., Stohl, A., and De Mazière, M.: Airborne DOAS measurements in Arctic: vertical distributions of aerosol extinction coefficient and NO<sub>2</sub> concentration, *Atmos. Chem. Phys.*, 11, 9219–9236, doi:10.5194/acp-11-9219-2011, 2011.
- Merlaud, A., Van Roozendaal, M., van Gent, J., Fayt, C., Maes, J., Toledo-Fuentes, X., Ronveaux, O., and De Mazière, M.: DOAS measurements of NO<sub>2</sub> from an ultralight aircraft during the Earth Challenge expedition, *Atmos. Meas. Tech.*, 5, 2057–2068, doi:10.5194/amt-5-2057-2012, 2012.
- Mickley, L., Jacob, D., Field, B., and Rind, D.: Climate response to the increase in tropospheric ozone since preindustrial times: A comparison between ozone and equivalent CO<sub>2</sub> forcings, *J. Geophys. Res.-Atmos.*, 109, D05106, doi:10.1029/2003JD003653, 2004.
- Millet, D. B., Guenther, A., Siegel, D. A., Nelson, N. B., Singh, H. B., de Gouw, J. A., Warneke, C., Williams, J., Eerdekens, G., Sinha, V., Karl, T., Flocke, F., Apel, E., Riemer, D. D., Palmer, P. I., and Barkley, M.: Global atmospheric budget of acetaldehyde: 3-D model analysis and constraints from in-situ and satellite observations, *Atmos. Chem. Phys.*, 10, 3405–3425, doi:10.5194/acp-10-3405-2010, 2010.
- Molina, M. J., Ivanov, A. V., Trakhtenberg, S., and Molina, L. T.: Atmospheric evolution of organic aerosol, *Geophys. Res. Lett.*, 31, L22104, doi:10.1029/2004GL020910, 2004.
- Myriokefalitakis, S., Vrekoussis, M., Tsigaridis, K., Wittrock, F., Richter, A., Brühl, C., Volkamer, R., Burrows, J. P., and Kanakidou, M.: The influence of natural and anthropogenic secondary sources on the glyoxal global distribution, *Atmos. Chem. Phys.*, 8, 4965–4981, doi:10.5194/acp-8-4965-2008, 2008.
- Oetjen, H., Baidar, S., Krotkov, N. A., Lamsal, L. N., Lechner, M., and Volkamer, R.: Airborne MAX-DOAS measurements over California: Testing the NASA OMI tropospheric NO<sub>2</sub> product, *J. Geophys. Res.-Atmos.*, 118, 13, 7400–7413, doi:10.1002/jgrd.50550, 2013.

- Parrella, J. P., Jacob, D. J., Liang, Q., Zhang, Y., Mickley, L. J., Miller, B., Evans, M. J., Yang, X., Pyle, J. A., Theys, N., and Van Roozendael, M.: Tropospheric bromine chemistry: implications for present and pre-industrial ozone and mercury, *Atmos. Chem. Phys.*, 12, 6723–6740, doi:10.5194/acp-12-6723-2012, 2012.
- Pierce, R. B. and Fairlie, T. D. A.: Chaotic advection in the stratosphere: Implications for the dispersal of chemically perturbed air from the polar vortex, *J. Geophys. Res.-Atmos.*, 98, 18589–18595, 1993.
- Pierce, R. B., Al-Saadi, J. A., Schaack, T., Lenzen, A., Zapotocny, T., Johnson, D., Kittaka, C., Buker, M., Hitchman, M. H., Tripoli, G., Fairlie, T. D., Olson, J. R., Natarajan, M., Crawford, J., Fishman, J., Avery, M., Browell, E. V., Creilson, J., Kondo, Y., and Sandholm, S. T.: Regional Air Quality Modeling System (RAQMS) predictions of the tropospheric ozone budget over east Asia, *J. Geophys. Res.*, 108, 8825, doi:10.1029/2002JD003176, 2003.
- Pierce, R. B., Schaack, T., Al-Saadi, J. A., Fairlie, T. D., Kittaka, C., Lingenfelter, G., Natarajan, M., Olson, J., Soja, A., Zapotocny, T., Lenzen, A., Stobie, J., Johnson, D., Avery, M. A., Sachse, G. W., Thompson, A., Cohen, R., Dibb, J. E., Crawford, J., Rault, D., Martin, R., Szykman, J., and Fishman, J.: Chemical data assimilation estimates of continental US ozone and nitrogen budgets during the Intercontinental Chemical Transport Experiment–North America, *J. Geophys. Res.-Atmos.*, 112, D12S21, doi:10.1029/2006JD007722, 2007.
- Piironen, P. and Eloranta, E. W.: Demonstration of a high-spectral resolution lidar based on an iodine absorption filter, *Opt. Lett.*, 19, 234–236, 1994.
- Platt, U. and J. Stutz: *Differential Optical Absorption Spectroscopy*, Springer, Heidelberg, 597 pp., 2008.
- Prados-Roman, C., Butz, A., Deutschmann, T., Dorf, M., Kritten, L., Minikin, A., Platt, U., Schlager, H., Sihler, H., Theys, N., Van Roozendael, M., Wagner, T., and Pfeilsticker, K.: Airborne DOAS limb measurements of tropospheric trace gas profiles: case studies on the profile retrieval of O<sub>4</sub> and BrO, *Atmos. Meas. Tech.*, 4, 1241–1260, doi:10.5194/amt-4-1241-2011, 2011.
- Puentedura, O., Gil, M., Saiz-Lopez, A., Hay, T., Navarro-Comas, M., Gómez-Pelaez, A., Cuevas, E., Iglesias, J., and Gomez, L.: Iodine monoxide in the north subtropical free troposphere, *Atmos. Chem. Phys.*, 12, 4909–4921, doi:10.5194/acp-12-4909-2012, 2012.
- Pundt, I., Pommereau, J.-P., Chipperfield, M., Van Roozendael, M., and Goutail, F.: Climatology of the stratospheric BrO vertical distribution by balloon-borne UV–visible spectrometry, *J. Geophys. Res.*, 107, 4806, doi:10.1029/2002JD002230, 2002.
- Read, K. A., Mahajan, A. S., Carpenter, L. J., Evans, M. J., Faria, B. V., Heard, D. E., Hopkins, J. R., Lee, J. D., Moller, S. J., Lewis, A. C., Mendes, L., McQuaid, J. B., Oetjen, H., Saiz-Lopez, A., Pilling, M. J., and Plane, M. C.: Extensive halogen-mediated ozone destruction over the tropical Atlantic Ocean, *Nature*, 453, 1232–1235, 2008.
- Richter, A., Wittrock, F., Ladstätter-Weissenmayer, A., and Burrows, J.: GOME measurements of stratospheric and tropospheric BrO, *Adv. Space Res.*, 29, 1667–1672, 2002.
- Rodgers, C. D.: *Inverse methods for atmospheric sounding: Theory and Practice*, Series on Atmospheric, Oceanic and Planetary Physics–Vol. 2, Singapore, World Scientific, 256 pp., 2000.
- Rodgers, C. D. and Connor, B. J.: Intercomparison of remote sounding instruments, *J. Geophys. Res.-Atmos.*, 108, 4116, doi:10.1029/2002JD002299, 2003.
- Rothman, L., Gordon, I., Barber, R., Dothe, H., Gamache, R., Goldman, A., Perevalov, V., Tashkun, S., and Tennyson, J.: HITEMP, the high-temperature molecular spectroscopic database, *J. Quant. Spectrosc. Ra.*, 111, 2139–2150, 2010.
- Rothman, L., Gordon, I., Babikov, Y., Barbe, A., Chris Benner, D., Bernath, P., Birk, M., Bizzocchi, L., Boudon, V., Brown, L., Campargue, A., Chance, K., Cohen, E. A., Coudert L. H., Devi, V. M., Drouin, B. J., Fayt, A., Flaud, J.-M., Gamache, R. R., Harrison, J. J., Hartmann, J.-M., Hill, C., Hodges, J. T., Jacquemart, D., Jolly, A., Lamouroux, J., Le Roy, R. J., Li, G., Long, D. A., Lyulin, O. M., Mackie, C. J., Massie, S. T., Mikhailenko, S., Müller, H. S. P., Naumenko, O. V., Nikitin, A. V., Orphal, J., Perevalov, V., Perrin, A., Polovtseva, E. R., Richard, C., Smith, M. A. H., Starikova, E., Sung, K., Tashkun, S., Tennyson, J., Toon, G. C., Tyuterev, V. I., and Wagner, G.: The HITRAN2012 molecular spectroscopic database, *J. Quant. Spectrosc. Ra.*, 130, 4–50, 2013.
- Saiz-Lopez, A., Lamarque, J.-F., Kinnison, D. E., Tilmes, S., Ordoñez, C., Orlando, J. J., Conley, A. J., Plane, J. M. C., Mahajan, A. S., Sousa Santos, G., Atlas, E. L., Blake, D. R., Sander, S. P., Schauffler, S., Thompson, A. M., and Brasseur, G.: Estimating the climate significance of halogen-driven ozone loss in the tropical marine troposphere, *Atmos. Chem. Phys.*, 12, 3939–3949, doi:10.5194/acp-12-3939-2012, 2012a.
- Saiz-Lopez, A., Plane, J. M. C., Baker, A. R., Carpenter, L. J., von Glasow, R., Martin, J. C. G., McFiggans, G., and Saunders, R. W.: *Atmospheric Chemistry of Iodine*, *Chem. Rev.*, 112, 1773–1804, 2012b.
- Salawitch, R. J., Weisenstein, D. K., Kovalenko, L. J., Sioris, C. E., Wennberg, P. O., Chance, K., Ko, M. K. W., and McLinden, C. A.: Sensitivity of ozone to bromine in the lower stratosphere, *Geophys. Res. Lett.*, 32, L05811, doi:10.1029/2004GL021504, 2005.
- Shipley, S. T., Tracy, D. H., Eloranta, E. W., Trauger, J. T., Sroga, J. T., Roesler, F. L., and Weinman, J. A.: A High Spectral Resolution Lidar to Measure Optical Scattering Properties of Atmospheric Aerosols, Part I: Instrumentation and Theory, *Appl. Optics*, 23, 3716–3724, 1983.
- Singh, H., Chen, Y., Staudt, A., Jacob, D., Blake, D., Heikes, B., and Snow, J.: Evidence from the Pacific troposphere for large global sources of oxygenated organic compounds, *Nature*, 410, 1078–1081, 2001.
- Singh, H. B., Salas, L. J., Chatfield, R. B., Czech, E., Fried, A., Walega, J., Evans, M. J., Field, B. D., Jacob, D. J., Blake, D., Heikes, B., Talbot, R., Sachse, G., Crawford, J. H., Avery, M. A., Sandholm, S., and Fuelberg, H.: Analysis of the atmospheric distribution, sources, and sinks of oxygenated volatile organic chemicals based on measurements over the Pacific during TRACE-P, *J. Geophys. Res.-Atmos.*, 109, D15S07, doi:10.1029/2003JD003883, 2004.
- Sinreich, R., Volkamer, R., Filsinger, F., Frieß, U., Kern, C., Platt, U., Sebastián, O., and Wagner, T.: MAX-DOAS detection of glyoxal during ICARTT 2004, *Atmos. Chem. Phys.*, 7, 1293–1303, doi:10.5194/acp-7-1293-2007, 2007.
- Sinreich, R., Coburn, S., Dix, B., and Volkamer, R.: Ship-based detection of glyoxal over the remote tropical Pacific Ocean,



- Atmos. Chem. Phys., 10, 11359–11371, doi:10.5194/acp-10-11359-2010, 2010.
- Spietz, P., Gómez Martín, J. C., and Burrows, J. P.: Spectroscopic studies of the I<sub>2</sub>O<sub>3</sub> photochemistry: Part 2. Improved spectra of iodine oxides and analysis of the IO absorption spectrum, *J. Photoch. Photobio. A*, 176, 50–67, 2005.
- Spinei, E., Cede, A., Herman, J., Mount, G. H., Eloranta, E., Morley, B., Baidar, S., Dix, B., Ortega, I., Koenig, T., and Volkamer, R.: Ground-based direct-sun DOAS and airborne MAX-DOAS measurements of the collision-induced oxygen complex, O<sub>2</sub>O<sub>2</sub>, absorption with significant pressure and temperature differences, *Atmos. Meas. Tech.*, 8, 793–809, doi:10.5194/amt-8-793-2015, 2015.
- Staudt, A. C., Jacob, D. J., Ravetta, F., Logan, J. A., Bachiochi, D., Krishnamurti, T. N., Sandholm, S., Ridley, B., Singh, H. B., and Talbot, B.: Sources and chemistry of nitrogen oxides over the tropical Pacific, *J. Geophys. Res.-Atmos.*, 108, 8239, doi:10.1029/2002JD002139, 2003.
- Sutton, R. T., Maclean, H., Swinbank, R., O'Neill, A., and Taylor, F.: High-resolution stratospheric tracer fields estimated from satellite observations using Lagrangian trajectory calculations, *J. Atmos. Sci.*, 51, 2995–3005, 1994.
- Thalman, R. and Volkamer, R.: Inherent calibration of a blue LED-CE-DOAS instrument to measure iodine oxide, glyoxal, methyl glyoxal, nitrogen dioxide, water vapour and aerosol extinction in open cavity mode, *Atmos. Meas. Tech.*, 3, 1797–1814, doi:10.5194/amt-3-1797-2010, 2010.
- Thalman, R. M. and Volkamer, R.: Temperature Dependent Absorption Cross-Sections of O<sub>2</sub>-O<sub>2</sub> collision pairs between 340 and 630 nm and at atmospherically relevant pressure, *Phys. Chem. Chem. Phys.*, 15, 15371–15381, doi:10.1039/c3cp50968k, 2013.
- Thalman, R., Zarzana, K. J., Tolbert, M. A., and Volkamer, R.: Rayleigh scattering cross-section measurements of nitrogen, argon, oxygen and air, *J. Quant. Spectrosc. Ra.*, 147, 171–177, doi:10.1016/j.jqsrt.2014.05.030, 2014.
- Thalman, R., Baeza-Romero, M. T., Ball, S. M., Borrás, E., Daniels, M. J. S., Goodall, I. C. A., Henry, S. B., Karl, T., Keutsch, F. N., Kim, S., Mak, J., Monks, P. S., Muñoz, A., Orlando, J., Peppe, S., Rickard, A. R., Ródenas, M., Sánchez, P., Seco, R., Su, L., Tyn-dall, G., Vázquez, M., Vera, T., Waxman, E., and Volkamer, R.: Instrument intercomparison of glyoxal, methyl glyoxal and NO<sub>2</sub> under simulated atmospheric conditions, *Atmos. Meas. Tech.*, 8, 1835–1862, doi:10.5194/amt-8-1835-2015, 2015.
- Theys, N., Van Roozendael, M., Hendrick, F., Fayt, C., Hermans, C., Baray, J.-L., Goutail, F., Pommereau, J.-P., and De Mazière, M.: Retrieval of stratospheric and tropospheric BrO columns from multi-axis DOAS measurements at Reunion Island (21° S, 56° E), *Atmos. Chem. Phys.*, 7, 4733–4749, doi:10.5194/acp-7-4733-2007, 2007.
- Theys, N., Van Roozendael, M., Hendrick, F., Yang, X., De Smedt, I., Richter, A., Begoin, M., Errera, Q., Johnston, P. V., Kreher, K., and De Mazière, M.: Global observations of tropospheric BrO columns using GOME-2 satellite data, *Atmos. Chem. Phys.*, 11, 1791–1811, doi:10.5194/acp-11-1791-2011, 2011.
- Thornberry, T. and Abbatt, J. P. D.: Heterogeneous reaction of ozone with liquid unsaturated fatty acids: detailed kinetics and gas-phase product studies, *Phys. Chem. Chem. Phys.*, 6, 84–93, 2004.
- Vandaele, A. C., Hermans, C., Simon, P. C., Carleer, M., Colin, R., Fally, S., Merienne, M.-F., Jenouvrier, A., and Coquart, B.: Measurements of the NO<sub>2</sub> absorption cross-section from 42 000 cm<sup>-1</sup> to 10 000 cm<sup>-1</sup> (238–1000 nm) at 220 K and 294 K, *J. Quant. Spectrosc. Ra.*, 59, 171–184, 1998.
- Van Roozendael, M., Wagner, T., Richter, A., Pundt, I., Arlander, D., Burrows, J., Chipperfield, M., Fayt, C., Johnston, P., Lambert, J.-C., Kreher, K., Pfeilsticker, K., Platt, U., Pommereau, J.-P., Sinnhuber, B.-M., Tornkvist, K. K., and Wittrock, F.: Intercomparison of BrO measurements from ERS-2 GOME, ground-based and balloon platforms, *Adv. Space. Res.*, 29, 1661–1666, doi:10.1016/S0273-1177(02)00098-4, 2002.
- Verma, S., Worden, J., Pierce, B., Jones, D. B. A., Al-Saadi, J., Boersma, F., Bowman, K., Eldering, A., Fisher, B., Jourdain, L., Kulawik, S., and Worden, H.: Ozone production in boreal fire smoke plumes using observations from the Tropospheric Emission Spectrometer and the Ozone Monitoring Instrument, *J. Geophys. Res.*, 114, D02303, doi:10.1029/2008JD010108, 2009.
- Vogel, L., Sihler, H., Lampel, J., Wagner, T., and Platt, U.: Retrieval interval mapping: a tool to visualize the impact of the spectral retrieval range on differential optical absorption spectroscopy evaluations, *Atmos. Meas. Tech.*, 6, 275–299, doi:10.5194/amt-6-275-2013, 2013.
- Volkamer, R., Molina, L. T., Molina, M. J., Shirley, T., and Brune, W. H.: DOAS measurement of glyoxal as an indicator for fast VOC chemistry in urban air, *Geophys. Res. Lett.*, 32, L08806, doi:10.1029/2005GL022616, 2005a.
- Volkamer, R., Spietz, P., Burrows, J. P., and Platt, U.: High-resolution absorption cross-section of Glyoxal in the UV/vis and IR spectral ranges, *J. Photoch. Photobio. A*, 172, 35–46, doi:10.1016/j.jphotochem.2004.11.011, 2005b.
- Volkamer, R., Coburn, S., Dix, B., and Sinreich, R.: The Eastern Pacific Ocean is a source for short lived atmospheric gases: Glyoxal and Iodine Oxide, *Clivar Exchanges*, 53, 30–33, 2010.
- Vrekoussis, M., Wittrock, F., Richter, A., and Burrows, J. P.: Temporal and spatial variability of glyoxal as observed from space, *Atmos. Chem. Phys.*, 9, 4485–4504, doi:10.5194/acp-9-4485-2009, 2009.
- Wagner, T., Leue, C., Wenig, M., Pfeilsticker, K., and Platt, U.: Spatial and temporal distribution of enhanced boundary layer BrO concentrations measured by the GOME instrument aboard ERS-2, *J. Geophys. Res.-Atmos.*, 106, 24225–24235, doi:10.1029/2002JD002139, 2001.
- Wagner, T., Dix, B., von Friedeburg, C., Friess, U., Sanghavi, S., Sinreich, R., and Platt, U.: MAX-DOAS O-4 measurements: A new technique to derive information on atmospheric aerosols – Principles and information content, *J. Geophys. Res.-Atmos.*, 109, D22205, doi:10.1029/2004JD004904, 2004.
- Wagner, T., Beirle, S., Brauers, T., Deutschmann, T., Frieß, U., Hak, C., Halla, J. D., Heue, K. P., Junkermann, W., Li, X., Platt, U., and Pundt-Gruber, I.: Inversion of tropospheric profiles of aerosol extinction and HCHO and NO<sub>2</sub> mixing ratios from MAX-DOAS observations in Milano during the summer of 2003 and comparison with independent data sets, *Atmos. Meas. Tech.*, 4, 2685–2715, doi:10.5194/amt-4-2685-2011, 2011.
- Wang, P., Richter, A., Bruns, M., Rozanov, V. V., Burrows, J. P., Heue, K.-P., Wagner, T., Pundt, I., and Platt, U.: Measurements of tropospheric NO<sub>2</sub> with an airborne multi-axis DOAS instrument, *Atmos. Chem. Phys.*, 5, 337–343, doi:10.5194/acp-5-337-2005, 2005.

- Wang, P., Richter, A., Bruns, M., Burrows, J. P., Scheele, R., Junkermann, W., Heue, K.-P., Wagner, T., Platt, U., and Pundt, I.: Airborne multi-axis DOAS measurements of tropospheric SO<sub>2</sub> plumes in the Po-valley, Italy, *Atmos. Chem. Phys.*, 6, 329–338, doi:10.5194/acp-6-329-2006, 2006.
- Waxman, E. M., Dzepina, K., Ervens, B., Lee-Taylor, J., Aumont, B., Jimenez, J. L., Madronich, S., and Volkamer, R.: Secondary organic aerosol formation from semi- and intermediate-volatility organic compounds and glyoxal: Relevance of O/C as a tracer for aqueous multiphase chemistry, *Geophys. Res. Lett.*, 40, 978–982, doi:10.1002/grl.50203, 2013.
- Wennberg, P. O., Brault, J. W., Hanisco, T. F., Salawitch, R. J., and Mount, G. H.: The atmospheric column abundance of IO: Implications for stratospheric ozone, *J. Geophys. Res.-Atmos.*, 102, 8887–8898, 1997.
- Wilmouth, D. M., Hanisco, T. F., Donahue, N. M., and Anderson, J. G.: Fourier transform ultraviolet spectroscopy of the A 2Π<sub>3/2</sub> – X 2Π<sub>3/2</sub> transition of BrO, *J. Phys. Chem. A.*, 103, 45, 8935–8945, 1999.
- Wittrock, F., Richter, A., Oetjen, H., Burrows, J. P., Kanakidou, M., Myriokefalitakis, S., Volkamer, R., Beirle, S., Platt, U., and Wagner, T.: Simultaneous global observations of glyoxal and formaldehyde from space, *Geophys. Res. Lett.*, 33, L16804, doi:10.1029/2006GL026310, 2006.
- WMO, World Meteorological Organization (WMO): Scientific Assessment of Ozone Depletion: 2010, WMO, Geneva, 2010.
- Yokouchi, Y., Osada, K., Wada, M., Hasebe, F., Agama, M., Murakami, R., Mukai, H., Nojiri, Y., Inuzuka, Y., Toom-Saunty, D., and Fraser, P.: Global distribution and seasonal concentration change of methyl iodide in the atmosphere, *J. Geophys. Res.-Atmos.*, 113, D18311, doi:10.1029/2008JD009861, 2008.
- Zaveri, R. A. and Peters, L. K.: A new lumped structure photochemical mechanism for large-scale applications, *J. Geophys. Res.*, 104, 30387–30415, doi:10.1029/1999JD900876, 1999.
- Zhou, S., Gonzalez, L., Leithead, A., Finewax, Z., Thalman, R., Vlasenko, A., Vagle, S., Miller, L. A., Li, S.-M., Bureekul, S., Furutani, H., Uematsu, M., Volkamer, R., and Abbatt, J.: Formation of gas-phase carbonyls from heterogeneous oxidation of polyunsaturated fatty acids at the air-water interface and of the sea surface microlayer, *Atmos. Chem. Phys.*, 14, 1371–1384, doi:10.5194/acp-14-1371-2014, 2014.
- Zhou, X. L. and Mopper, K.: Apparent Partition-Coefficients of 15 Carbonyl-Compounds Between Air and Seawater and Between Air and Fresh-Water – Implications for Air Sea Exchange, *Environ. Sci. Technol.*, 24, 1864–1869, 1990.
- Zondlo, M. A., Paige, M. E., Massick, S. M., and Silver, J. A.: Vertical cavity laser hygrometer for the National Science Foundation Gulfstream-V aircraft, *J. Geophys. Res.-Atmos.*, 115, D20309, doi:10.1029/2010JD014445, 2010.